Seismic tomography of the Arctic region: inferences for the thermal structure and evolution of the lithosphere

SERGEI LEBEDEV[1]*, ANDREW J. SCHAEFFER[2], JAVIER FULLEA[1] & VICTORIA PEASE[3]

[1]*Geophysics Section, School of Cosmic Physics, Dublin Institute for Advanced Studies, 5 Merrion Square, Dublin 2, Ireland*

[2]*Department of Earth and Environmental Sciences, University of Ottawa, Ottawa K1N 6N5, Canada*

[3]*Department of Geological Sciences, Stockholm University, Stockholm 106 91, Sweden*

**Correspondence: sergei@cp.dias.ie*

Abstract: Waveform tomography with very large datasets reveals the upper-mantle structure of the Arctic in unprecedented detail. Using tomography jointly with computational petrology, we estimate temperature in the lithosphere–asthenosphere depth range and infer lithospheric structure and evolution. Most of the boundaries of the mantle roots of cratons in the Arctic are coincident with their geological boundaries at the surface. The thick lithospheres of the Greenland and North American cratons are separated by a corridor of thin lithosphere beneath Baffin Bay and through the middle of the Canadian Arctic Archipelago; the southern archipelago is part of the North American Craton. The mantle root of the cratonic block beneath northern Greenland may extend westwards as far as central Ellesmere Island. The Barents and Kara seas show high velocities indicative of thick lithosphere, similar to cratons. The locations of intraplate basaltic volcanism attributed to the High Arctic Large Igneous Province are all on thin, non-cratonic lithosphere. The lithosphere beneath the central part of the Siberian Traps is warmer than elsewhere beneath the Siberian Craton. This observation is consistent with lithospheric erosion associated with the large igneous province volcanism. A corridor of relatively low seismic velocities cuts east–west across central Greenland. This indicates lithospheric thinning, which appears to delineate the track of the Iceland hotspot.

Supplementary material: Figures with comparisons of different tomographic models at 50 and 200 km depths are available at https://doi.org/10.6084/m9.figshare.c.3817810

The Arctic region is composed of lithospheric blocks with very different properties and very different tectonic histories (Fig. 1). The continental units range in age from Archean cratons to Phanerozoic orogens (e.g. Pease 2011; Pease *et al.* 2014). The deep water High Arctic includes the Canada Basin, probably >100 myr old, and the younger Eurasia Basin associated with modern spreading along the Gakkel Ridge (Herron *et al.* 1974; Gaina *et al.* 2015). The intraplate basaltic volcanism of the Cretaceous High Arctic Large Igneous Province (HALIP) has disrupted and modified the pre-existing lithosphere across a broad area (Tarduno 1998; Saumur *et al.* 2016). The Cenozoic opening of the adjacent North Atlantic was accompanied by volcanism at and near the Iceland hotspot. Hotspot activity is likely to have affected the thermal evolution of both the oceanic lithosphere and the continental margins of the North Atlantic (e.g. White & Lovell 1997; Anell *et al.* 2009; Maupin *et al.* 2013).

Understanding the structure and evolution of the different tectonic units – and of their interrelationships within the Arctic region as a whole – requires an understanding of the structure and evolution of the entire lithospheric plates, from the crust to the lithospheric mantle. The mechanical behaviour of the lithosphere depends on its temperature and thickness (e.g. McKenzie *et al.* 2005; Eaton *et al.* 2009); other important parameters include the solidus, which depends on the rock composition and volatile content (e.g. Katz *et al.* 2003). The temperature and thickness of the lithosphere are closely related. The bottom of the thermal lithosphere (the lithosphere–asthenosphere boundary) is defined by the depth near which the steep, conductive geotherm that characterizes the lithosphere meets the mantle adiabat that characterizes the convecting asthenosphere below (Fig. 2) (e.g. Pollack & Chapman 1977; Jaupart & Mareschal 1999).

Both the temperature and strength of the lithosphere also depend on the thickness and

From: Pease, V. & Coakley, B. (eds) 2018. *Circum-Arctic Lithosphere Evolution*. Geological Society, London, Special Publications, **460**, 419–440.
First published online July 6, 2017, https://doi.org/10.1144/SP460.10

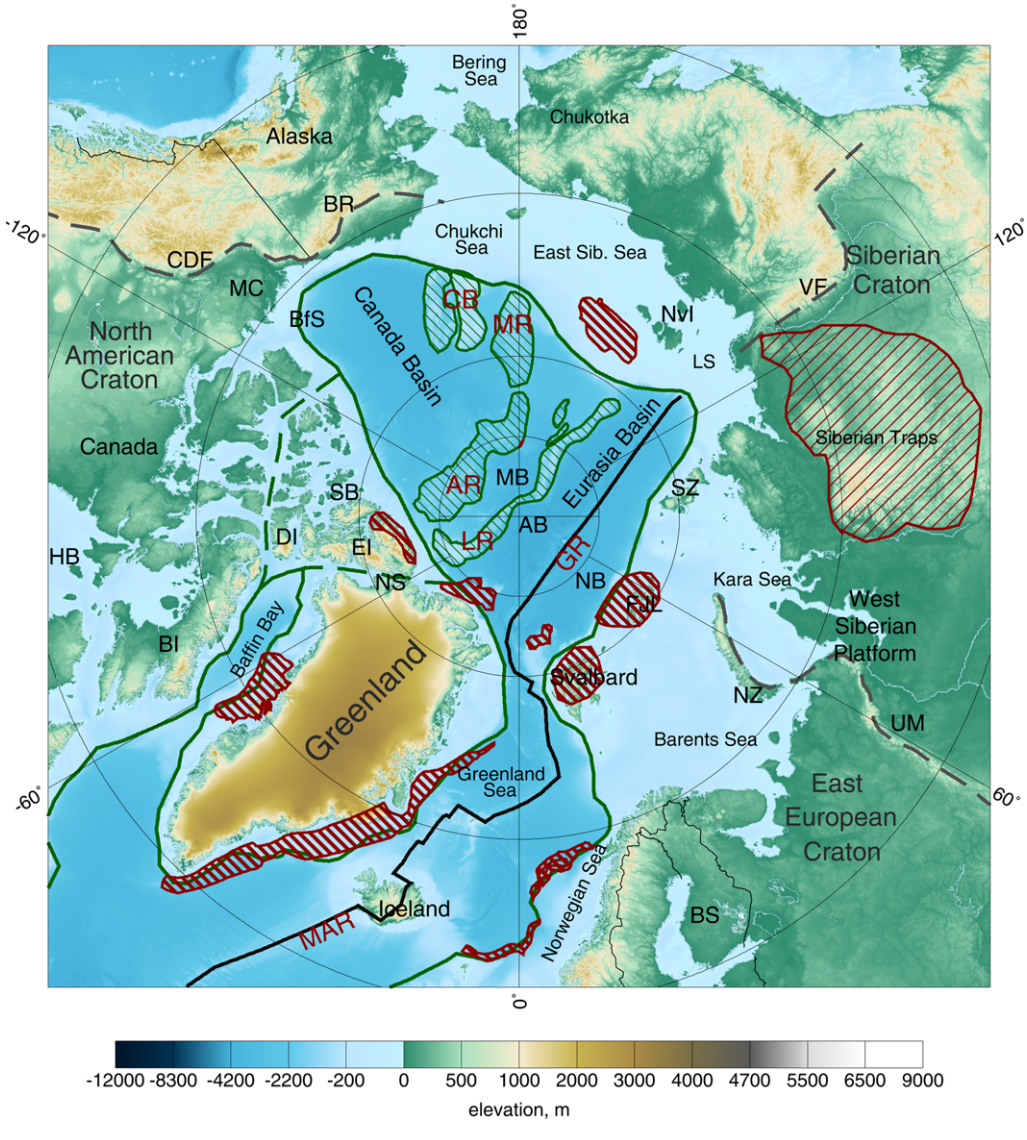

Fig. 1. Topographic map of the Arctic region. Ridges on the High Arctic seafloor are shown as green hatched areas; locations of intraplate volcanism are shown as red hatched areas (Gaina *et al.* 2014; Schiffer *et al.* 2017). AB, Amundsen Basin; AR, Alpha Ridge; BfS, Beaufort Sea; BI, Baffin Island; BR, Brooks Range; BS, Baltic Shield; CB, Chukchi Borderlands; CDF, Cordilleran Deformation Front; DI, Devon Island; EI, Ellesmere Island; FJL, Franz Josef Land; HB, Hudson Bay; LR, Lomonosov Ridge; LS, Laptev Sea; MAR, Mid-Atlantic Ridge; MB, Makarov Basin; MC, Mackenzie Craton; MR, Mendeleev Ridge; NB, Nansen Basin; NvI, Novosibirsk Islands; NZ, Novaya Zemlya; SB, Sverdrup Basin; SZ, Severnaya Zemlya; UM, Ural Mountains; VF, Verkhoyansk Fold Belt.

composition of the crust. Radiogenic heat production in thick continental crust results in the continental lithosphere being warmer than oceanic lithosphere of the same thickness, with the latter producing little heat within its thin basaltic crust (Fig. 2). Colder lithosphere is generally stiffer, although the mechanical behaviour of the lithosphere also depends on the strength layering within it (e.g. Burov & Watts 2006).

Because the lithosphere is cooled at the Earth's surface, it will tend to grow in thickness until its lower portion becomes negatively buoyant and sinks into the underlying mantle (e.g. Bird 1979; Houseman & Molnar 1997). The thickness of the

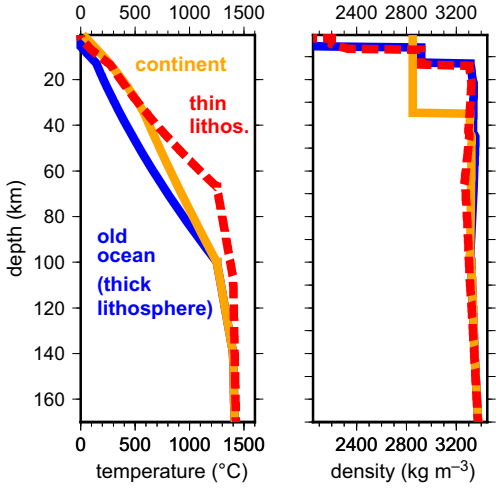

Fig. 2. Type profiles of the temperature and density beneath an old ocean with a 100 km thick lithosphere, a young ocean with a 60 km thick lithosphere and a layer of sediments on top of the crystalline crust, and a Phanerozoic continent with a 100 km thick lithosphere.

lithosphere thus reaches a maximum, and this maximum is determined by the composition of the lithospheric mantle. The lithosphere beneath Archean cratons is compositionally buoyant as a result of its depletion in basaltic components (e.g. Jordan 1975, 1988) and therefore it has a greater thickness than lithosphere elsewhere (e.g. Artemieva 2006; Sodoudi *et al.* 2013). Seismic tomography models (which map the variations in temperature-dependent seismic velocities), show the cold, thick lithospheres of cratons as prominent high-velocity anomalies, seen down to depths of 200–250 km (e.g. French *et al.* 2013; Schaeffer & Lebedev 2015*a*; Debayle *et al.* 2016).

Phanerozoic mantle lithosphere, in contrast, is less depleted and lacks the compositional buoyancy to grow as thick as the lithosphere of Archean cratons. The maximum thickness of Phanerozoic lithosphere has been estimated as *c.* 150 km (Poudjom Djomani *et al.* 2001), with a more typical thickness of, probably, *c.* 100 km. Tomographic models show seismic velocities within Phanerozoic lithosphere that are substantially lower than those within the cratonic Archean lithosphere, reflecting much higher temperatures within the former.

Oceanic lithosphere appears to cool and thicken nearly monotonically from its origin at a mid-ocean ridge to its subduction (e.g. Maggi *et al.* 2006; Schaeffer & Lebedev 2013; Burgos *et al.* 2014). This cooling can be interrupted by the plate passing over a mantle hotspot, which will reheat the lithosphere; subsequently, the plate will resume its cooling and thickening. The flattening of the bathymetry of old (>80 myr) oceans, and the apparent lack of correlation of heat flow at their surface with lithospheric age, have suggested that the thickness of the oceanic lithosphere reaches a maximum when the seafloor is *c.* 80 myr old (the plate model, e.g. Stein & Stein 1992, 2015). Interestingly, seismic velocity structure and azimuthal anisotropy show evidence of the lithosphere continuing to grow in thickness with age along the isotherms of the half-space cooling model (Davis & Lister 1974), without reaching a maximum (Becker *et al.* 2014; Schaeffer *et al.* 2016); these different lines of evidence still need to be reconciled.

The lithospheric temperature and thickness beneath both continents and oceans reflect the age and evolution of the lithosphere. A craton, a Phanerozoic platform and an active orogen will usually have distinctly different lithospheric temperatures and thicknesses, as will an old or a young part of an ocean basin. This has been demonstrated by global tectonic regionalizations based solely on tomography, with no *a priori* information (Lekic & Romanowicz 2011; Schaeffer & Lebedev 2015*a*). In continents, the deep lithospheric boundaries mapped by these regionalizations are coincident, in most cases, with the geological boundaries between tectonic blocks of different ages mapped at the surface. (For a detailed discussion of the boundaries within the North American continent, in particular, see Schaeffer & Lebedev (2014).) In oceans, seismic velocities within the lithosphere show a consistent increase with the age of the oceanic crust. Lithospheric temperatures can thus inform us of the properties and histories of tectonic terranes and of the locations of the boundaries between them.

The relatively sharp lateral thermal gradients at the boundaries between lithospheric blocks survive for tens and hundreds of millions of years, in spite of thermal diffusion across the boundaries. This is because the dominant heat-exchange pattern in the system is the cooling of the lithosphere from above, at the Earth's surface. The thickness of the lithosphere of each block is in dynamic equilibrium: it will thicken as a result of cooling from above, but if it becomes thicker than its equilibrium thickness, it will then thin as the negatively buoyant lower portions of the lithosphere sink into the underlying asthenosphere. Thus the lithospheres of cratons, anomalously thick as a result of their compositional buoyancy, can indefinitely maintain steady-state lithospheric geotherms that are colder than those within the thinner lithosphere of neighbouring Phanerozoic blocks.

Most Archean cratons in existence today preserve their characteristically thick mantle lithosphere, but there are a few well-documented exceptions. For example, the mantle lithosphere of the

eastern Sino-Korean Craton, thick in the Palaeozoic Era, had undergone significant thinning by the Cenozoic Era, possibly due to processes associated with continental collision or subduction (e.g. Menzies *et al.* 1993; Lebedev & Nolet 2003). A mantle plume can also modify and thin cratonic lithosphere: the impact of a thermochemical mantle plume has been modelled to cause lithospheric erosion (Sobolev *et al.* 2011). In the Arctic region, major hotspots are known to have interacted with the lithospheres of Greenland, which is probably crossed by the Iceland hotspot track, and the Siberian Craton (the Siberian Traps large igneous province (LIP)). Here, we present new seismic evidence for the modification and thinning of parts of the lithosphere of the Greenland and Siberian cratons by hotspots.

Lateral variations in temperature within the mantle lithosphere can be inferred from seismic velocities. In addition to temperature, seismic velocities also depend on the composition of the rock and on the presence of water or partial melt within it. The effect of compositional variations in the mantle is much smaller than that of temperature, however. It can account for $<1\%$ of the variation in the velocity of shear waves (e.g. Deschamps *et al.* 2002; Schutt & Lesher 2006), whereas the positive shear-velocity anomalies beneath cratons, for example, reach 8–10% above the global average (Lebedev *et al.* 2009; Agius & Lebedev 2013). At the opposite end of the range, seismic velocities can be $>10\%$ below average values beneath mid-ocean ridges and intraplate volcanic areas (e.g. Schaeffer & Lebedev 2015*a*). In these locations, the lithosphere is thin and hot and the seismic velocities are lowered further by partial melting, in particular in the top 100 km of the mantle (e.g. Hammond & Humphreys 2000). In the back-arc regions of subduction zones, partial melting is enhanced by water released into the mantle from the subducting oceanic crust (e.g. Katz *et al.* 2003).

Anomalies in shear wave velocities mapped by tomography can thus offer an immediate qualitative estimate of the temperature heterogeneity of the lithosphere. In order to determine temperature from seismic velocity at a given depth quantitatively, the sensitivity of elastic and anelastic properties of realistic rock compositions to temperature must be evaluated (e.g. Karato 1993; Sobolev *et al.* 1996; Goes *et al.* 2000; Cammarano *et al.* 2003). Computational petrological modelling (e.g. Connolly 2005; Afonso *et al.* 2008; Fullea *et al.* 2009) enables the calculation of density, seismic velocities, attenuation and other properties as a function of rock composition, temperature and pressure based on extensive thermodynamic databases. Such modelling offers a self-consistent framework for relating seismic and other data to the physical properties of the entire lithosphere.

In this study, we use new waveform tomography of the Arctic to obtain new evidence on the evolution of the lithospheric blocks in the region, the location of the boundaries between them and dynamic processes at depth. In addition to using the heterogeneity in seismic velocity directly, we also use computational petrology to calculate lateral variations in temperature and to estimate lithospheric geotherms beneath selected locations in the High Arctic.

Seismic tomography

As a result of the explosive recent growth of global and regional seismic networks, increasingly detailed models of the lithosphere and the underlying upper mantle are now possible at scales ranging from regional to global. To take advantage of the resolving power of the very large datasets now available, we must apply methods that (1) can extract highly complete structural information from each seismogram and (2) are automated, so that all the relevant data can be processed.

Waveform tomography

Waveform tomography is an effective approach for imaging the entire crust and upper mantle at a regional or global scale (e.g. Nolet 1990; Lebedev *et al.* 1997; Lebedev & Nolet 2003; Legendre *et al.* 2012; Schaeffer & Lebedev 2013, 2014). We invert seismic waveforms that include the fundamental mode surface waves (which travel along the surface of the Earth and sense different depth ranges depending on their periods) and S- and multiple S-waves (which dive deeper into the mantle and have complementary depth sensitivities that depend on the distance from the source to the station and the order of the multiple). Regional S- and multiple S-waves are often triplicated and, also, can interfere with each other and with the fundamental mode on the seismogram. By inverting the entire seismic waveform, we can extract information simultaneously from all these waves without the need to separate their arrivals.

The Automated Multimode Inversion (AMI) of surface and S-wave forms (Lebedev *et al.* 2005) performs automated, accurate processing of large numbers of broadband seismograms. Each successful waveform inversion produces a set of linear equations with uncorrelated uncertainties (Nolet 1990) that describe one-dimensional perturbations in elastic structure within a finite width sensitivity volume between the earthquake and the station. The perturbations are with respect to a three-dimensional reference model (Lebedev & van der Hilst 2008), including a three-dimensional crustal

model, CRUST2.0 (Bassin *et al.* 2000; http://igppweb.ucsd.edu/~gabi/crust2.html). All the linear equations are then solved together for three-dimensional perturbations in the isotropic S and P velocities with respect to the three-dimensional reference model and for the 180° periodic azimuthal anisotropy of the S velocity. The broad period range of the fundamental mode surface waves (10–400 s) and the complementary sensitivities of the regional S and multiple S-waves provide resolution from the crust down to the deep upper mantle, including the entire lithosphere–asthenosphere depth range.

Our new tomographic model, AMISvArc, is a global, shear wave velocity model of the upper mantle and crust constructed using the same waveform tomography methods and data handling approaches as the recently published SL2013sv, SV2013NA and SL2016SvA models (Schaeffer & Lebedev 2013, 2014, 2015*a*; Schaeffer *et al.* 2016), but incorporating additional data, particularly in and around the Arctic region (Fig. 3). There are no stations in the central, sea-covered part of the High Arctic, but because we use the surface and regional body waves traversing between the various sources and

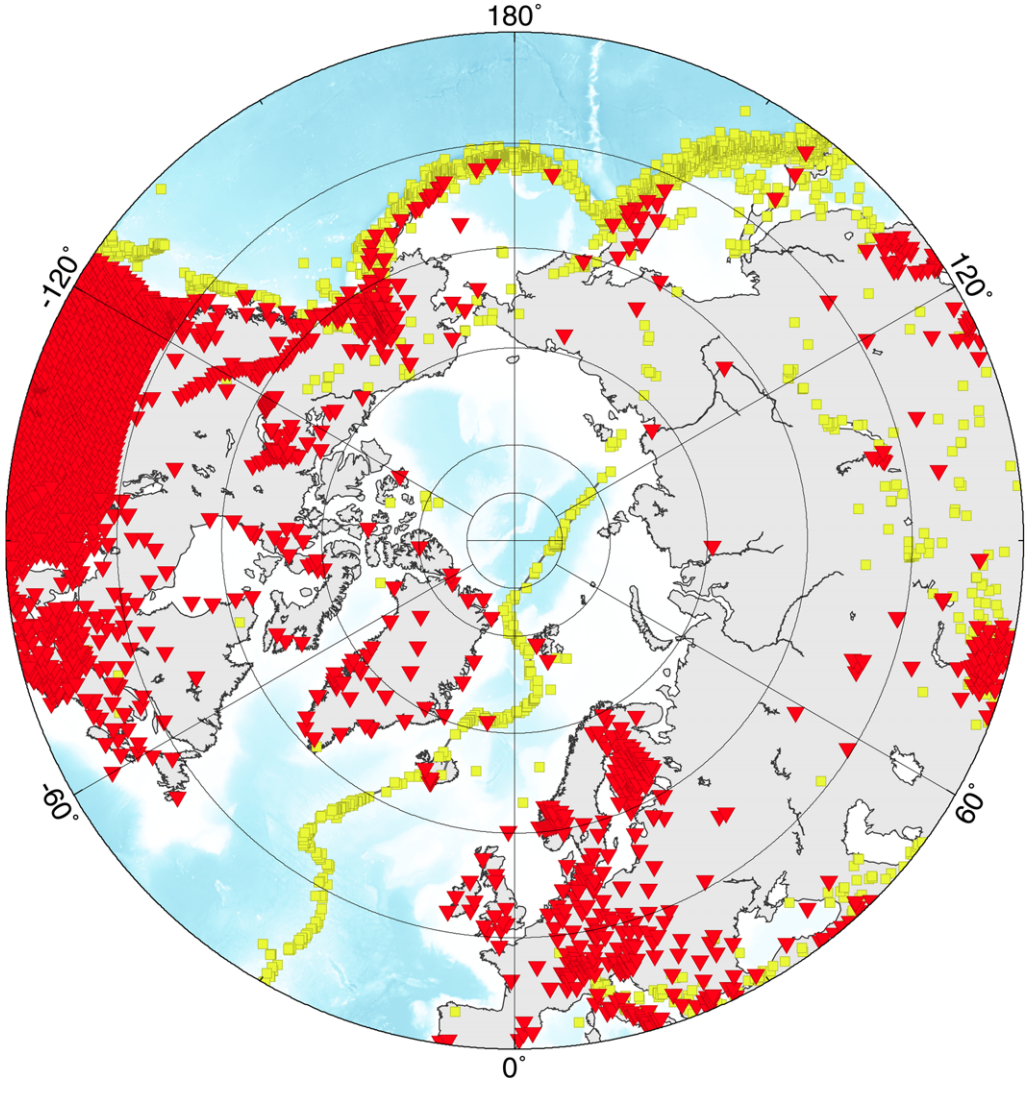

Fig. 3. Broadband seismic stations (inverted triangles) and earthquakes (small squares) in and around the Arctic region. These sources and stations were used in the waveform tomography model of the Arctic along with our global set of stations and earthquakes (Schaeffer & Lebedev 2014; Schaeffer *et al.* 2016).

stations, we have dense coverage across the entire region. A further technical description and validation of the tomographic model are presented elsewhere (Schaeffer & Lebedev, 2015*b*; Schaeffer, A.J., Lebedev, S. & Gaina, C., Structure of the Circum-Arctic lithosphere and asthenosphere imaged using multimode waveform tomography, Tectonophysics, Invited Research Paper, in prep.); a description of the waveform tomography methods can be found in Lebedev *et al.* (2005) and Lebedev & van der Hilst (2008). In the following, we focus on the inferences on the lithospheric structure of the Arctic region offered by this model.

S-wave velocity variations in the lithosphere and asthenosphere

Figure 4 shows map views of our model at depths in the shallow upper mantle. At 30–60 km, the cold lithosphere of the Canada Basin, origin of which is debated (Pease *et al.* 2014; Chian *et al.* 2016), dominates the High Arctic. S-wave velocities (V_s) here are similar to those within old (>100 myr old) oceanic lithosphere around the world (Schaeffer & Lebedev 2015*a*). V_s here is substantially higher than beneath the younger Eurasia Basin and also higher than beneath the continental margins of the Canada Basin, where the uppermost mantle is likely to be warmer due to radiogenic heating within the continental crust.

At 80–110 km depth, cratons are the dominant high-velocity anomalies. In most cases, the deep boundaries of the cratonic roots in the mantle closely follow the boundaries mapped at the surface (e.g. Pease *et al.* 2014). A few significant exceptions to this are discussed in the following.

At 150 km and deeper (Fig. 5), there is no longer a visible contrast in seismic velocities between the central Canada Basin and the Eurasia Basin. Instead, a continuous low-velocity anomaly stretches from one basin to the other – an image of the asthenosphere beneath the High Arctic. This low-velocity anomaly, corresponding to the High Arctic asthenosphere, is significantly smaller in amplitude than the anomaly beneath the North Atlantic in the vicinity of the Iceland hotspot. Here in the NE Atlantic, the extremely low velocities indicate extensive partial melting in the uppermost mantle (confirmed by our calculations in this paper).

A high-velocity anomaly stands out at depths >100 km in the SE corner of the Canada Basin, adjacent to the thick, cold lithosphere of the Mackenzie Craton (Schaeffer & Lebedev 2014), the NW extremity of the North American Craton. (We use 'the Mackenzie Craton' here as a formal term, having presented convincing seismic evidence for its existence previously (Schaeffer & Lebedev 2014).) The anomaly is seen beneath the Beaufort Sea and also extends to the west and to the east of this sea (Fig. 5, 150–330 km).

Comparison of tomographic models

Figures 6 and 7 show a comparison of recent global upper mantle and whole mantle models at depths of 100 and 150 km, respectively (see Supplementary figures for 50 and 200 km depth comparisons). Each model is plotted with respect to its own global mean at each depth. The reference model used in tomographic inversions will usually be different from the eventual global mean of the model, hence the slight difference in the appearance of AMISvArc in Figures 4 and 5, where it is plotted with respect to its reference model, and in Figures 6 and 7, where it is plotted with respect to its global mean.

All the tomographic models were constrained by datasets that included surface waves, particularly sensitive to variations in the S-wave velocities in the lithospheric depth range (Bartzsch *et al.* 2011; Lebedev *et al.* 2013). Some of the models also included waveforms of regional S and multiple S-waves (including our AMISvArc, top left panels), surface wave higher mode measurements or teleseismic body wave arrival times. The quantity of data and station coverage vary substantially between the models (with AMISvArc using the most complete current station coverage in and around the Arctic, Fig. 3), as do the inversion schemes.

The comparison shows which features are consistently mapped by all the models. These include, for example, the mantle roots of the North American, East European and Siberian cratons, where the thick, cold lithosphere is characterized by high seismic velocities, seen as dark blue and purple colours (Figs 6 & 7). All the models also show the warm High Arctic asthenosphere and the hot asthenosphere beneath Iceland.

As we focus on smaller spatial scales, the models differ. For example, all the models show a relatively thick lithosphere beneath the Barents Sea, but the distributions of the high-velocity anomalies beneath the sea, laterally and with depth, vary from one model to another (see also the figures in the Supplementary material). The V_s distribution here is also different in published regional surface wave tomography (Levshin *et al.* 2001, 2007). The regional Barents Sea model of Levshin *et al.* (2007), not plotted here, shows high-velocity lithosphere beneath both the western and eastern Barents Sea, as in the other models, but their highest velocities at 60 km depth are in the SW part of the sea and at 100–160 km in the SE part of the sea, similar to model CUB (Shapiro & Ritzwoller 2002) but different from the other plotted models. The Barents Sea presents a challenge for all tomographic studies

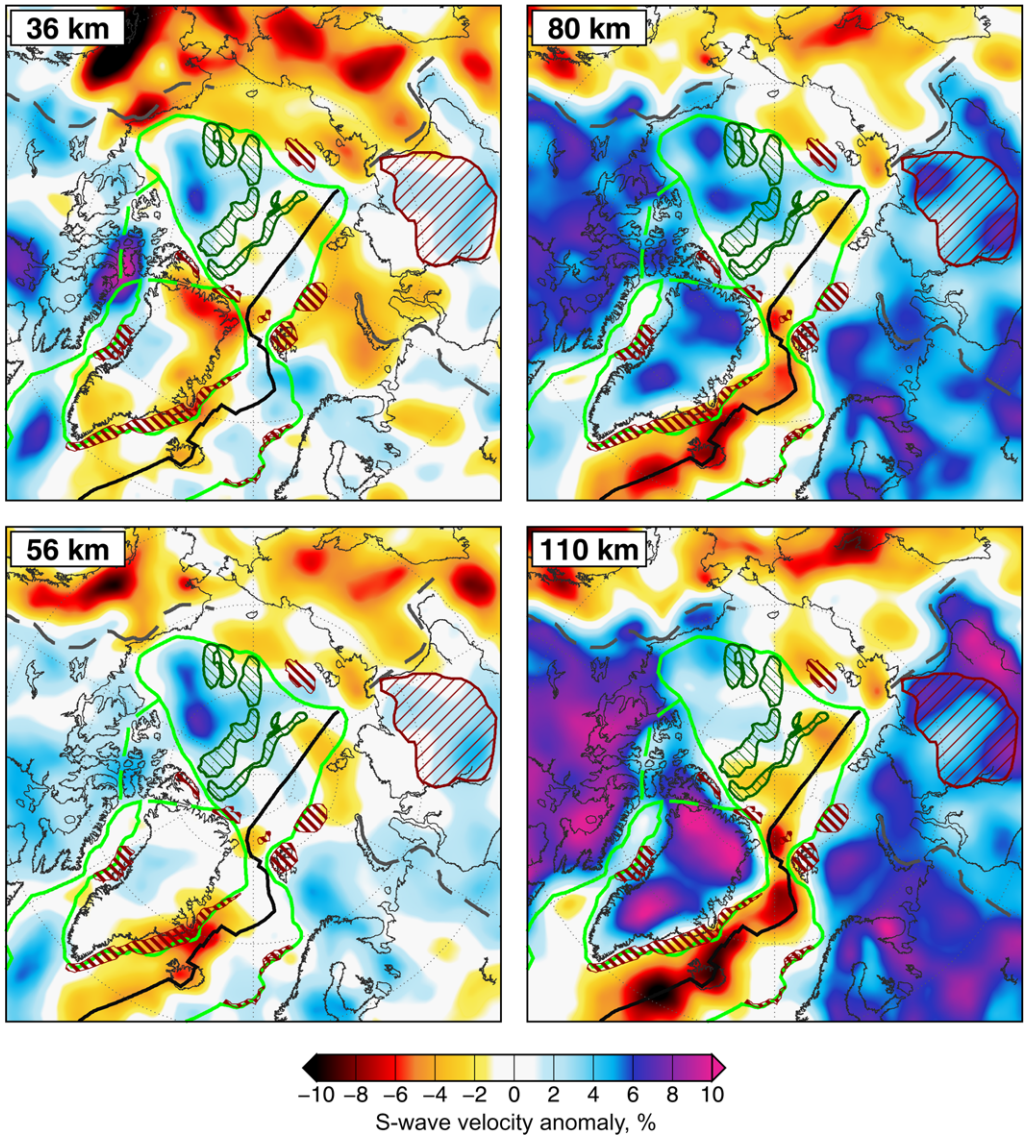

Fig. 4. Map views of our tomographic model at four depths in the shallow upper mantle. The reference values of the vertically polarized S-wave velocity in the mantle are: 4.46 km s^{-1} at 36 km depth; 4.42 km s^{-1} at 56 km depth; and 4.38 km s^{-1} at 80 and 110 km depths. Where the depths shown fall within the crust, the reference values are those of CRUST2.0 (Bassin *et al.* 2000; http://igppweb.ucsd.edu/~gabi/crust2.html), smoothed at its block boundaries. The reference S-wave velocity values and deviations are at the reference period 50 s. Tectonic and volcanic features are as in Figure 1.

because of the very thick layer of sediments across much of it, which, if not known and accounted for accurately, will affect the seismic velocity at the lithospheric depths in the models. Fine-scale regional crustal models will probably need to be incorporated into the tomography with large, Arctic-scale datasets for different models to show more agreement in the variations in lithospheric structure beneath and around the Barents Sea.

Some models (e.g. Savani, S40RTS; Figs 6 & 7) are very smooth, whereas others include smaller scale structures. For the most part, the models are mutually consistent at large scales. As we move to the finer scale structures – seen, in particular, in

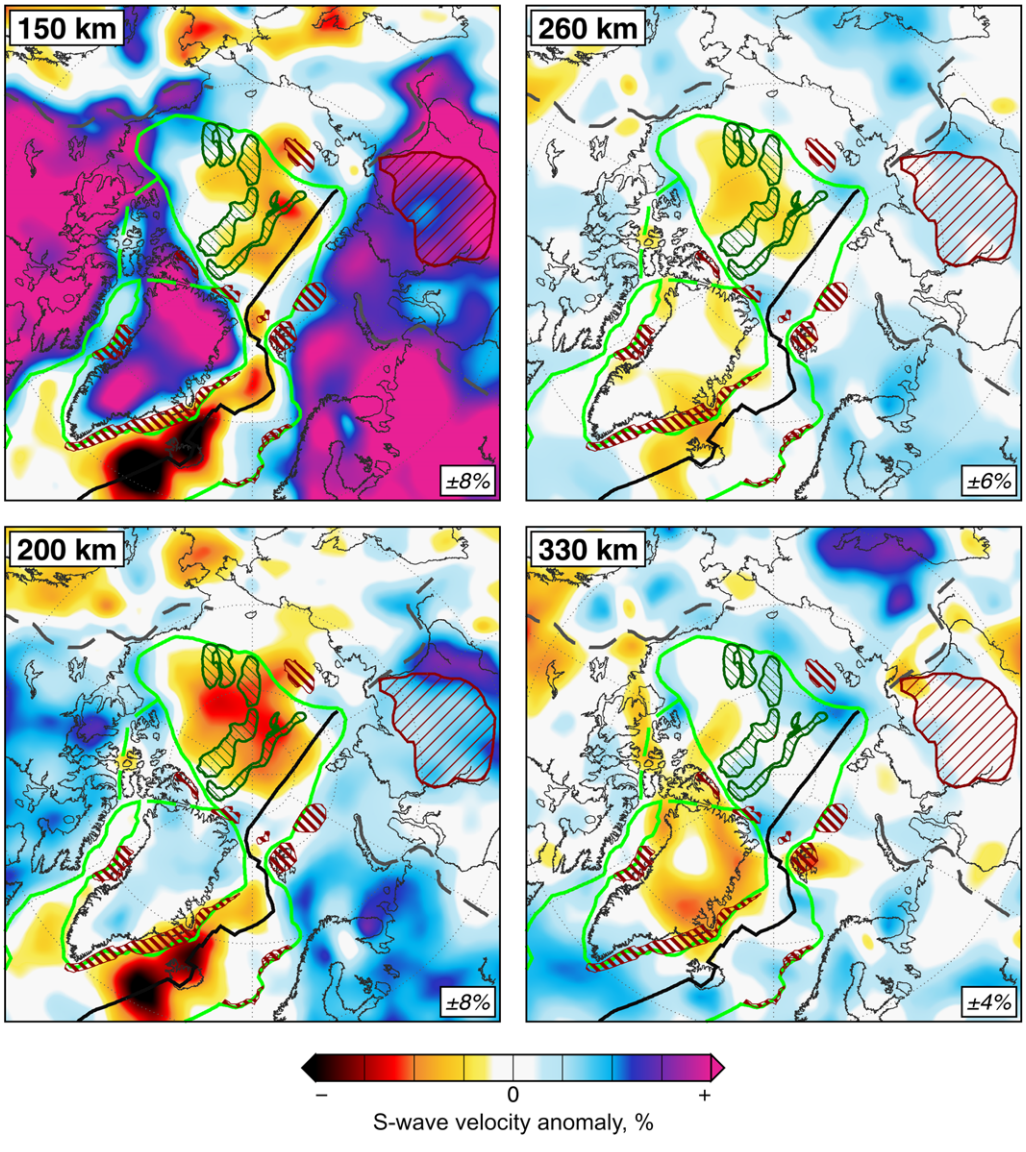

Fig. 5. Map views of our tomographic model at four depths in the deeper upper mantle. The reference values of the vertically polarized S-wave velocity in the mantle are: 4.39 km s^{-1} at 150 km; 4.45 km s^{-1} at 200 km; 4.62 km s^{-1} at 250 km; and 4.75 km s^{-1} at 330 km depth. The reference S-wave velocity values and deviations are at the reference period 50 s. Tectonic and volcanic features are as in Figure 1.

AMISvArc – many regional-scale features are more clearly distinct and present clearer evidence on the regional structure and evolution of the lithosphere. Examples of such regional-scale features include the corridor of relatively low velocities separating the cratonic roots of the Greenland and North American cratons, the low-velocity corridor cutting east–west across central Greenland and the thinning of the lithosphere beneath the central part of the Siberian Traps.

Mapping lithospheric temperature

For a rock of a given composition at a given pressure (P) and temperature (T), we can calculate the

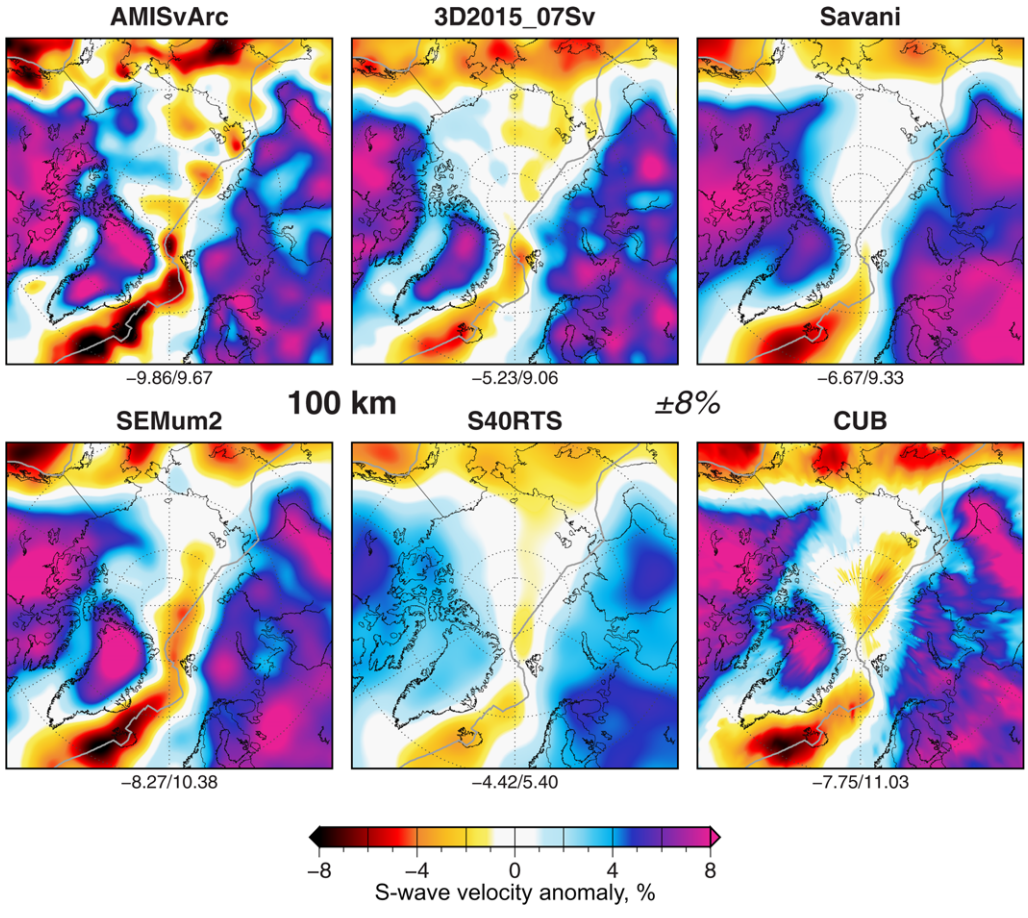

Fig. 6. A comparison of vertically polarized S-wave velocity distributions at 100 km depth in the Arctic region according to different global tomographic models: AMISvArc (Schaeffer & Lebedev 2015*b*; this study); 3D2015_07Sv (Debayle *et al.* 2016); Savani (Auer *et al.* 2014); SEMum2 (French *et al.* 2013); S40RTS (Ritsema *et al.* 2011); and CUB (Shapiro & Ritzwoller 2002). Each model is plotted with respect to its own global mean at the depth.

shear wave velocity within it, the attenuation (important because it affects the V_s–T relationship) and other properties (e.g. Connolly 2005; Fullea *et al.* 2012; Vozar *et al.* 2014). A V_s distribution such as that in Figures 4 and 5 can therefore be inverted to give the distribution of temperature if we assume reasonable, representative compositions for the mantle lithosphere and asthenosphere. If the composition and rock properties that control attenuation are fixed, then there is a non-linear, but unique, one-to-one relationship between T and V_s. The V_s–T inversion can thus be recast as a simple conversion by pre-calculating V_s for the entire relevant range of temperature, pressure and composition.

The solutions of the tomographic inverse problem are non-unique and many different models can fit the data equally well. Specifically, our data tightly constrain the values of V_s in relatively broad depth ranges, but poorly constrain small-scale radial variations in V_s. Thus instead of converting V_s values at a given single depth to T at this depth, we determine an average value of T over a depth range. The depth range should be sufficiently broad for the average temperature values within it to be robust. It should also capture the variations in lithospheric properties across the region. (Alternatively, we could reduce the non-uniqueness of seismic models during the course of their construction, either by introducing petrological constraints into the inversions or by formulating them as thermodynamic inversions from the beginning (e.g. Khan *et al.* 2009, 2011; Fullea *et al.* 2012; Afonso *et al.* 2013). The development of thermodynamic inversion methods for large waveform datasets is the subject of ongoing work.)

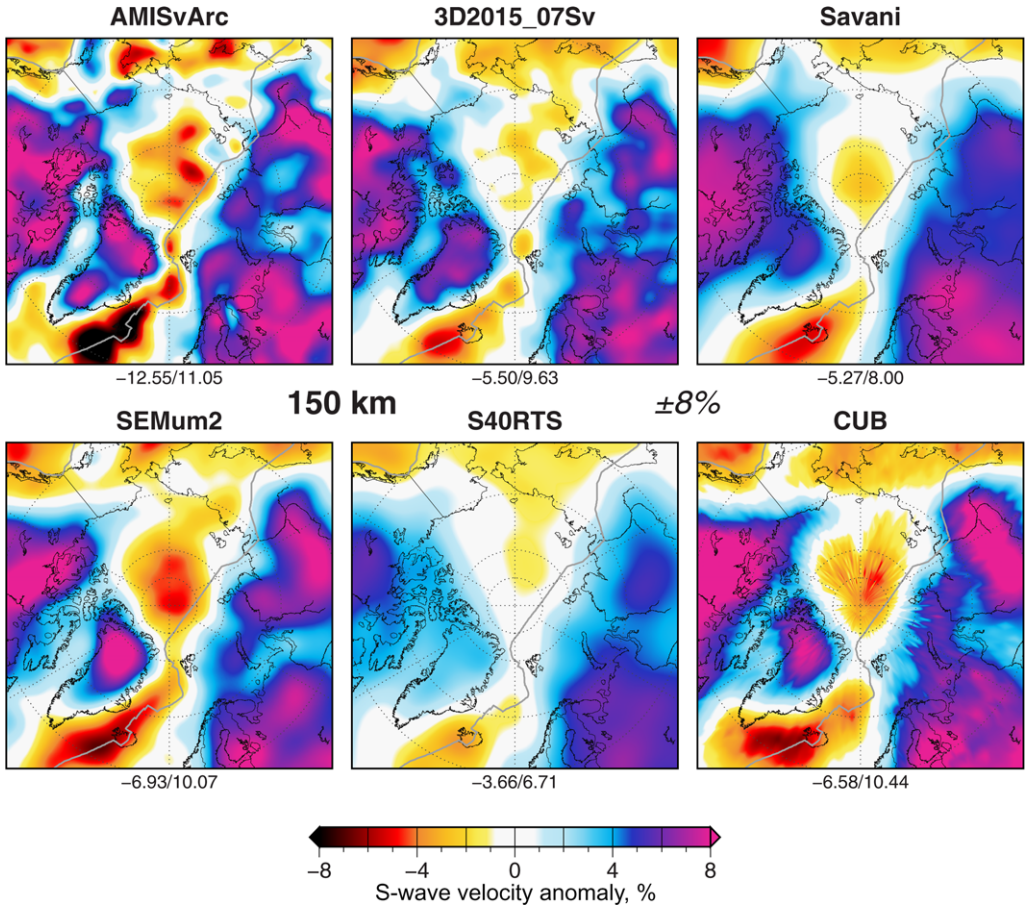

Fig. 7. A comparison of vertically polarized S-wave velocity distributions at 150 km depth in the Arctic region according to different global tomographic models (as in Fig. 6). Each model is plotted with respect to its own global mean at the depth.

Figure 8 shows the average temperature in the 80–150 km depth range. It is determined as an average of the temperature values calculated from V_s (Figs 4 & 5) at each depth within the range. The composition of the upper mantle at a point is assumed to fall into one of the three lithospheric compositional domains corresponding to the tectonothermal ages: Phanerozoic, Proterozoic or Archean. The domains are defined geographically by means of lithospheric regionalization based on our tomographic model (see map in Schaeffer & Lebedev 2015*a*). (Taking the composition into account increases the accuracy of the V_s–T conversion, but this has only a minor effect because of the much smaller dependence of V_s on composition than on temperature. The main patterns in Figure 8 would not change if the composition was not taken into account). A representative composition has been assigned to each domain based on the global average compositions from xenoliths and peridotite massifs (Griffin *et al.* 2009). Radially, the mantle composition varies from that of a lithospheric type (any of the three mentioned earlier) to a typical sublithospheric, pristine upper mantle composition (model PUM, McDonough & Sun 1995) (Table 1). For composition only, an average lithospheric thickness is assumed for each of the three compositional domains. In the Phanerozoic and Proterozoic terranes, the depth to the base of the layer with a lithospheric composition is set to 120 km. In the cratons the composition is 'Archaean' from the base of the crust down to 120 km and 'Proterozoic' from 120 km down to 200 km depth.

The V_S–T inversion is based on the thermodynamically self-consistent T–P tables (for each of the mantle compositions in Table 1) containing V_s values pre-calculated using the computational petrology software package Perple_X (Connolly

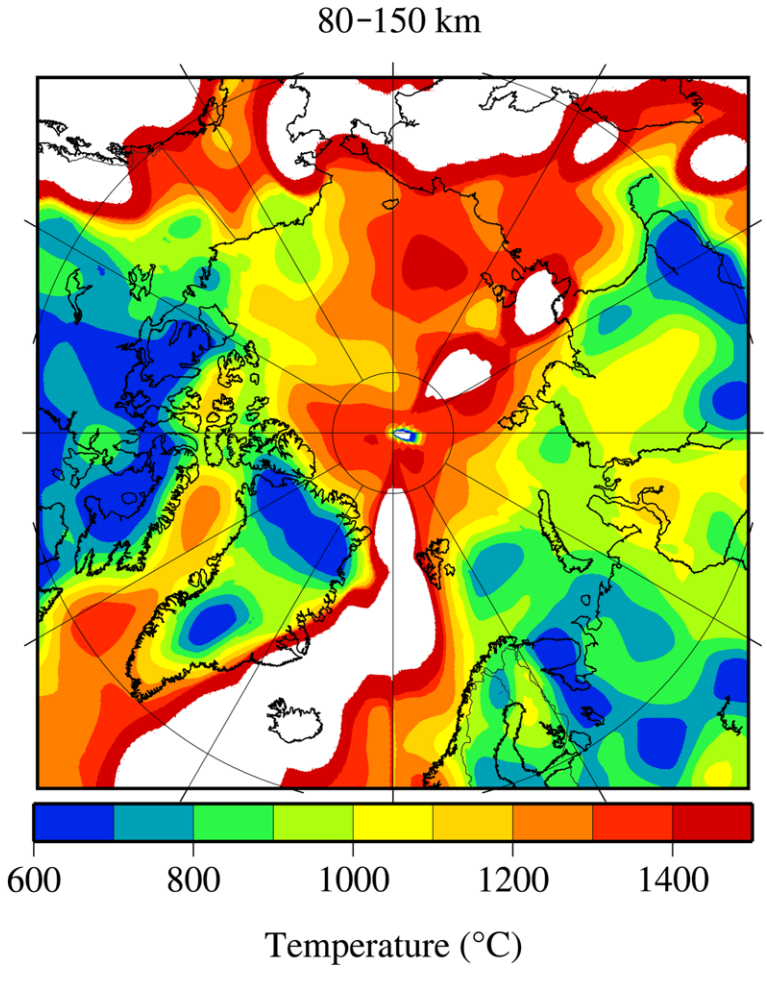

Fig. 8. Average temperature in the 80–150 km depth range derived from our tomographic model. White areas: locations where partial melting is likely to occur at least at some of the depths within the range. Partial melting at a depth is inferred if the temperature obtained from the V_s inversion exceeds the mantle peridotite dry solidus (Katz *et al.* 2003) at the corresponding pressure.

2005). The V_s values are corrected to account for the effect of attenuation. We compute the anelasticity as a T–P-dependent correction to the anharmonic output velocities from Perple_X (e.g. Minster & Anderson 1981; Karato 1993; Afonso *et al.* 2005). The values for grain size and activation volume in the anelasticity correction applied here are taken from Fullea *et al.* (2012), where they are investigated and discussed in detail.

The white areas in Figure 8 show locations where partial melting is likely to occur at least at some of the depths in the 80–150 km range. Partial melting is inferred if the temperature obtained from the V_s inversion exceeds the mantle peridotite dry solidus (Katz *et al.* 2003) at the corresponding pressure.

A useful reference for the interpretation of Figure 8 is given by steady-state geotherms, computed as described in the following section. A 260 km thick cratonic lithosphere, for example, has an average temperature within the 80–150 km depth range of 740°C. For a continent with a 100 km thick lithosphere (Fig. 2), the average calculated temperature is 1277°C.

Lithospheric geotherms

We now use the integrated geophysical–petrological software LitMod (Afonso *et al.* 2008; Fullea *et al.* 2009) to compute the vertical profiles of

Table 1. *Bulk mantle compositions used in this work from xenolith suites and peridotite massifs*

	Average Phanerozoic (wt%)*	Average Proterozoic (wt%)*	Average Archean (wt%)*	PUM M&S95 (wt%)†
SiO_2	44.5	44.6	45.7	45
TiO_2	0.14	0.07	0.04	0.201
Al_2O_3	3.5	1.9	0.99	4.45
Cr_2O_3	0.4	0.4	0.28	0.384
FeO	8.0	7.9	6.4	8.05
MnO	0.13	0.12	0.11	0.135
MgO	39.8	42.6	45.5	37.8
CaO	3.1	1.7	0.59	3.55
Na_2O	0.24	0.12	0.07	0.36
NiO	0.26	0.26	0.3	
Mg#	89.9	90.6	92.7	89.3

*Global average values taken from Griffin *et al.* (2009).
†PUM, primitive upper mantle; M&S95 refers to McDonough & Sun (1995).

temperature and density. The lithospheric geotherm is computed under the assumption of steady-state heat transfer in the lithospheric mantle, considering a P–T-dependent thermal conductivity in the mantle and prescribed thermal parameters in the crust (Table 2). The geotherm in the convecting sub-lithospheric mantle is given by an adiabatic temperature gradient. A transitional buffer layer is located just beneath the bottom of the lithosphere, connecting the lithosphere and the convecting sub-lithospheric mantle. This transitional buffer layer is characterized by a continuous linear super-adiabatic gradient – that is, heat transfer is controlled by both conduction and convection; see Fullea *et al.* (2009) for details.

Stable mineral assemblages in the mantle are calculated using a Gibbs free energy minimization as described by Connolly (2005). The composition is defined within the major oxide system NCFMAS (Na_2O–CaO–FeO–MgO–Al_2O_3–SiO_2). All the stable assemblages are computed using a modified and augmented version (Afonso & Zlotnik 2011) of the thermodynamic database of Holland & Powell (1998). The density in the mantle is determined from the elastic moduli and density of each end-member mineral as described by Connolly & Kerrick (2002) and Afonso *et al.* (2008). For a detailed description of the core Gibbs energy minimization scheme used to determine stable mineral phase assemblages, see Connolly & Kerrick (2002); for a detailed description of the averaging scheme used to compute whole-rock properties (in particular, seismic velocities and density), see Afonso *et al.* (2008).

The calculations are for the entire lithospheric column and therefore also produce values for the isostatic topography, surface heat flow and other observable variables (e.g. Fullea *et al.* 2012). The oceanic models in Figure 2 show a 5.5 km seafloor depth for the 'old ocean' with a dense, 100 km thick lithosphere and a 2 km seafloor depth for the 'young ocean' with a 60 km thick lithosphere and a 4 km thick layer of sediment. The latter model was designed to be similar to that of the Nansen Basin, the southern half of the slowly opening Eurasia Basin adjacent to Eurasia's continental margin.

Figure 9 compares the profile of the central Canada Basin with those of a non-cratonic continent (100 km thick lithosphere) and a hypothetical profile that we computed for the Beaufort Sea, set up to fit the seismic and other observations as closely as possible. For the central Canada Basin,

Table 2. *Assumed geophysical properties of different crustal layers*

Layer	Density (kg m^{-3})	Heat production (W m^{-3})	Thermal conductivity (W m^{-1} K^{-1})
Oceanic sediments	2200	$1.2\ 10^{-6}$	3
Oceanic crust	2920	$1\ 10^{-7}$	2.1
Continental Crust	2850	$0.7\ 10^{-6}$	2.5
Beaufort Sea sediments	2400–2700	$2\ 10^{-6}$	3
Beaufort Sea crust	2950	$1\ 10^{-7}$	2.1

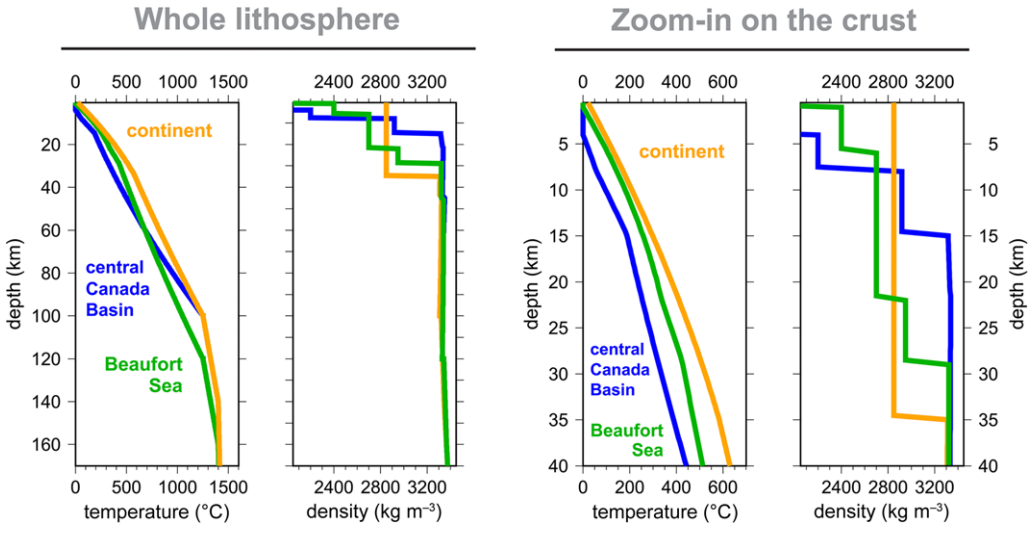

Fig. 9. Estimated profiles of temperature and density beneath the central Canada Basin and the Beaufort Sea compared with those of a Phanerozoic continent with a 100 km thick lithosphere.

a one-dimensional model with a steady-state geotherm and a 100–120 km lithospheric thickness can fit both the V_s values from our tomographic model and the observed bathymetry. For the SE part of the basin (the Beaufort Sea), in contrast, the observations are difficult to fit with a steady-state one-dimensional model. The seismic velocities here are relatively low in the uppermost mantle (similar to those in a Phanerozoic continental region), but relatively high at 100–200 km depth and deeper.

We attempted to construct a one-dimensional physical model that could reproduce these V_s variations while keeping the bathymetry consistent with observations. A model with a 120 km thick lithosphere and a thick layer of sediments with high heat production goes some way towards explaining the relatively high temperatures in the uppermost mantle and relatively low temperatures at greater depths, but it cannot quite match the variations in seismic velocity. This suggests that the high velocities at depths >100 km may be due to the cooling of the upper mantle by the adjacent Mackenzie Craton, the NW extremity of the North American Craton (Schaeffer & Lebedev 2014). The three-dimensionality of the thermal regime is why one-dimensional steady-state models are insufficient to explain the V_s values beneath the Beaufort Sea.

Arctic lithospheric structure: a brief overview

The seismic velocity and thermal structure of the Arctic upper mantle offers abundant evidence for the architecture and evolution of the lithosphere across the region. We now highlight a few selected, robust observations, with an emphasis on the more unexpected – or less well-understood – features.

Canada Basin

The seismic velocity and thermal structure of the Canada Basin lithosphere is similar to that of old oceans. The origin of the basin is debated, with end-member models invoking normal seafloor spreading, the stretching of continental crust and exhumation and serpentinization of the upper mantle; all three mechanisms may have contributed to the formation of the basin at different locations and at different times (e.g. Lawver & Scotese 1990; Lane 1997; Drachev & Saunders 2006; Grantz *et al.* 2011; Mosher *et al.* 2012; Koulakov *et al.* 2013; Pease *et al.* 2014; Chian *et al.* 2016). Our one-dimensional, lithospheric-scale physical modelling shows that the inferred temperature within the lithosphere, the bathymetry of the basin and the thickness of its sedimentary cover (Jakobsson *et al.* 2012; Petrov *et al.* 2016) are consistent with it having a normal oceanic, basaltic crystalline crust with a thickness of *c.* 7 km. On the basis of the one-dimensional modelling, however, we cannot rule out the possibility that such a crust could have been formed by a mechanism other than normal seafloor spreading. Regarding the age of the lithosphere, the temperature profile inferred from the high seismic velocities within it indicates that it has been cooling for >100 myr. The S-wave velocities here are similar to those within old (>100 myr)

oceanic lithosphere around the world (see Schaeffer & Lebedev 2015*a*).

Eurasia Basin

The younger and narrower Eurasia Basin shows lower seismic velocities and higher temperatures than the Canada Basin. In contrast with the Mid-Atlantic Ridge in the North Atlantic, where partial melting is inferred in a broad corridor along its entire length, the ultra-slow-spreading Gakkel Ridge in the Eurasia Basin (e.g. Coakley & Cochran 1998) shows partial melting beneath only a few of its segments, one of them just north of the Fram Strait that separates the North Atlantic and Eurasia basins.

A continuous low-velocity anomaly extends through the Fram Strait from the North Atlantic to beneath the adjacent, westernmost portion of the Gakkel Ridge. The extent of this anomaly may indicate how far the hot North Atlantic asthenosphere has flowed northwards. Schmidt-Aursch & Jokat (2016) used three-dimensional gravity modelling to infer that the separation of Greenland from Svalbard (forming the Fram Strait at chron C5/C6) led to the inflow of North Atlantic mantle into the western Eurasia Basin, creating a distinct pattern of magmatism along the Gakkel Ridge.

Our tomographic model presents an image of the inflow of hot North Atlantic asthenosphere into the Eurasia Basin. It suggests a major effect of the inflow on the character of the seafloor spreading. The northern limit of the observed low-velocity anomaly (Fig. 4, 80–110 km) is at around 84° N and this is where a boundary is observed between the Western Volcanic Zone of the Gakkel Ridge to the south, with basalts covering the seafloor and with well-developed magmatic characteristics similar to those of slow-spreading ridges elsewhere, and the Sparsely Magmatic Zone to the north, with little evidence for magmatism and a predominantly peridotitic crust (Thiede *et al.* 2002; Jokat *et al.* 2003; Michael *et al.* 2003; Schlindwein *et al.* 2007).

Craton–ocean boundaries

Both the southern half of the Eurasia Basin (the Nansen Basin) and the southern portion of the Canada Basin (the Beaufort Sea) are bordered to the south by thick, cold continental lithosphere. Both locations show high-velocity anomalies at 150–200 km depth, indicating upper mantle that is colder than the mantle beneath the rest of the basins further north. This is likely to be due to cooling by the adjacent cold continental lithosphere. The resulting negative temperature anomaly in the deep upper mantle – and the associated positive density anomaly – is likely to have caused an extra amount of subsidence of the basins during the course of their evolution (Fullea *et al.* 2012) and contributed to the development of their thick sedimentary layers.

Cratons

The boundaries of the deep roots of the East European and Siberian cratons, as seen in the high S-wave velocities in the mantle (Figs 4 & 5, 110 and 150 km depths), roughly follow the geological boundaries at the surface (e.g. Pease *et al.* 2014). To the north, the Barents and Kara Sea also show high velocities indicative of thick lithosphere, similar to that of the cratons.

The heterogeneity in seismic velocity beneath the Baltic Shield reveals pronounced lateral variations in the thickness of the lithosphere within it. These have been reported previously in a number of studies; different models, however, continue to show substantially different variations in lithospheric thickness (e.g. Bruneton *et al.* 2004; Artemieva *et al.* 2006; Weidle & Maupin 2008; Legendre *et al.* 2012; Pedersen *et al.* 2013; this study).

In the NW corner of the North American Craton, our tomography delineates the westwards lateral extent of the cratonic lithosphere. The recently identified Mackenzie Craton (Schaeffer & Lebedev 2014), unexposed at the surface, forms the northwestern extremity of the North American Craton and extends roughly to the front of the Rockies (Schaeffer & Lebedev 2014).

The deep cratonic root of Greenland is separated from the root of the North American Craton by tectonic units without a thick cratonic lithosphere. West of central Greenland, the two are separated by Baffin Bay, with its warmer, thinner oceanic lithosphere. The corridor of thin lithosphere underlying Baffin Bay continues westwards into the Canadian Arctic Archipelago.

Canadian Arctic Archipelago

The southern part of the Canadian Arctic Archipelago – the islands to the north of the North America mainland and between North America and Greenland – is clearly a part of the North American Craton, with high seismic velocities indicative of cold, thick lithosphere, continuous with that beneath mainland Canada.

The Sverdrup Basin in the northern part of the archipelago (Fig. 1) is a major Carboniferous to Palaeogene depocentre (Stephenson *et al.* 1987; Embry & Beauchamp 2008, Midwinter *et al.* 2016), with sedimentary thicknesses in the 5–15 km range (Petrov *et al.* 2016). According to our models, the lithosphere is relatively thick in the southern part of the basin and thins to the north; the axis of the basin (Embry & Beauchamp 2008)

coincides roughly with the 1000°C isotherm (the transition from green to yellow) in Figure 8. The area to the south of the Sverdrup Basin (including the Devon, Somerset, Cornwallis, Bathurst and Melville islands) shows a thinner lithosphere and mostly thin (<1 km) or absent sedimentary cover (Petrov *et al.* 2016). Subsidence and sedimentation within the Sverdrup Basin are thus likely to reflect the cooling and thickening of the Phanerozoic mantle lithosphere, whereas the lithosphere just south of the Sverdrup Basin is thin and there has been little subsidence and sedimentation. This causal relationship – also seen in other parts of the world (Meier *et al.* 2016) – is due to the fact that thicker (and colder) mantle lithosphere is denser than thinner (and warmer) lithosphere (Fig. 2). Unless the lithosphere is strongly depleted and compositionally buoyant, as in Archean cratons, and provided that the crustal structure remains the same, thickening of the mantle lithosphere thus has to cause subsidence (see Fullea *et al.* 2012 for more detail and illustrations).

The corridor of thin lithosphere that cuts through the archipelago south of the Sverdrup Basin connects to Baffin Bay near Devon Island. Here, Burke & Dewey (1973) postulated a plume-generated, Devon Island triple junction, noting that a junction in this location had also been recognized earlier by Wegener (1929) and Wilson (1963). The three arms of this proposed junction were Baffin Bay (between Greenland and North America) to the SE, the Nares Strait (between Greenland and Ellesmere Island) to the north and Lancaster Sound (between Devon and Baffin islands) to the west. Burke & Dewey (1973) suggested that the Lancaster Sound arm became inactive before reaching the spreading stage – unlike the Baffin Bay arm, where seafloor spreading has formed the oceanic lithosphere now separating Greenland from North America. The Nares Strait arm, underlain by continental crust (e.g. Altenbernd *et al.* 2016), was proposed to accommodate left-lateral transform motion.

New plate reconstructions of the Palaeogene motion of Greenland and the region between Canada and Greenland show total extension across northern Baffin Bay of *c.* 175 km and total stretching across the Lancaster Sound Basin of only 40 km (Oakey & Chalmers 2012). According to these reconstructions, the southeastern part of Ellesmere Island is part of the Greenland plate.

Our results show pronounced thinning of the lithosphere beneath the corridor between the Sverdrup Basin to the north and the bulk of the North American Craton to the south, highlighting the importance of the failed rift here. No lithospheric thinning is observed beneath the Nares Strait between Greenland and Ellesmere Island.

Ellesmere Island

At 150 km depth (Fig. 5), the entire southeastern-central part of Ellesmere Island shows high velocities that are continuous with those beneath cratonic northwestern Greenland. Northern Ellesmere Island, by contrast, is underlain by lower velocities, indicative of thinner lithosphere. At 110 km depth (Fig. 4), the seismic velocities beneath the central-southeastern part of the island are also high, but not as high as beneath Greenland. The inferred average lithospheric temperature (Fig. 8) suggests that the central Ellesmere Island lithosphere is not as cold as that of northern Greenland. However, it is as cold as cratonic lithosphere in many locations elsewhere.

Although the southeastern part of the island is known to be a part of the Canadian–Greenland Shield, the central part of the island is covered by Neoproterozoic, Cambrian and Devonian shelf deposits (e.g. Saalmann *et al.* 2005). Our images suggest that the cratonic lithosphere – forming a single lithospheric block with northern Greenland – may extend beneath both southeastern and central Ellesmere Island.

The crustal structure of central and northern Ellesmere Island presents a record of deformation associated with the assembly and subsequent break-up of the Late Palaeozoic–Mesozoic continent of Laurasia (Piepjohn *et al.* 2015; Schiffer & Stephenson 2017). The Ellesmerian fold-and-thrust belt stretches from the west to the NE of the island and is thought to have formed during the early Carboniferous accretion of a terrane that is now the northernmost part of Ellesmere Island to the northern margin of Laurasia (southeastern part of the island). Most structures of the Ellesmerian orogeny were later reactivated or overprinted by folding and (thrust and strike-slip) faulting during the Cenozoic Eurekan deformation, related to the final break-up of Laurasia and the opening of the Labrador Sea and Baffin Bay. The presence of cold lithosphere beneath central Ellesmere Island suggests that the stiff mantle lithosphere of the cratonic margin may have underthrusted the accreting crust during the Ellesmerian orogeny.

The inferred lateral extent of cratonic lithosphere beneath the island puts limits on where the relative motions between Greenland and (parts of) Ellesmere Island may occur (the Nares Strait debate, e.g. Dawes & Kerr 1982; Saalmann *et al.* 2005). It provides evidence against major displacement along Nares Strait, which is consistent with many Precambrian and Palaeozoic structures continuing without offset from Greenland across Nares Strait to Ellesmere Island (e.g. Dawes *et al.* 1982; Dawes & Kerr 1982).

Thin lithosphere and intraplate volcanism

All the locations of the intraplate basaltic volcanism attributed to the HALIP are underlain by relatively thin, non-cratonic lithosphere. This is demonstrated by the seismic velocities beneath them being much lower than the velocities beneath cratons (Fig. 4, 80 and 110 km depths). For example, northern Ellesmere Island has thin, warm lithosphere with low seismic velocities. It is in this northern part of the island that the Cretaceous alkaline basaltic volcanism associated with HALIP has been identified (Fig. 1) and strong mafic underplating has been reported (Stephenson *et al.* 2017). The presence of thick lithosphere beneath the central and southeastern part of the island, as shown by our tomography, is consistent with the volcanism being limited to the northern part of the island. Even if anomalously hot asthenosphere was placed beneath the entire island – or beneath its central part – it would flow towards the locations with thinner lithosphere along the lithosphere–asthenosphere boundary and undergo significant partial melting when it reached relatively shallow depths (Thompson & Gibson 1991; Morgan & Morgan 2005; Lebedev *et al.* 2006), that is, beneath the northern part of Ellesmere Island.

Siberian Traps

The Permo-Triassic Siberian Traps represent one of the largest continental LIPs on Earth. They erupted rapidly at around 248 Ma and are thought to be centred on thick cratonic lithosphere (e.g. Renne & Basu 1991; Dobretsov *et al.* 2013; Kuskov *et al.* 2014; Cherepanova & Artemieva 2015), with significant magmatism also occurring beyond the boundaries of the Siberian Craton (e.g. Reichow *et al.* 2002; Kuzmichev & Pease 2007). Our model shows that the lithosphere beneath the central part of the LIP is, in fact, warmer and thinner than that beneath the surrounding parts of the Siberian Craton.

The thinning of cratonic lithosphere by a hot mantle plume has been modelled specifically for the Siberian Traps case, with the model invoking extensive plume melting and erosion of the thick cratonic lithosphere at the time of emplacement of the traps (Sobolev *et al.* 2011). Our images map the location where lithospheric thinning associated with the LIP probably took place. We note that this LIP is not associated with the HALIP, nor is it likely to be associated with the Iceland plume (Torsvik 2016; Torsvik *et al.* 2016).

Iceland plume track across Greenland?

A corridor of relatively low seismic velocities cuts across central Greenland from west to east (Figs 4 & 5, 110, 150 km; Figs 6 & 7, top left), indicating that the lithosphere within this corridor is thinner and warmer than normal cratonic lithosphere. We cannot exclude the possibility that the lithosphere here has been thinner than typical cratonic lithosphere since the assembly of the Greenland landmass. The tectonic boundaries within the interior of ice-covered Greenland are uncertain. It is thought, however, that central Greenland – through which the low-velocity corridor cuts – is occupied by the Archean Rae Craton (e.g. St-Onge *et al.* 2009). The corridor of thin lithosphere may thus be a result of the modification of the lithosphere within the craton that post-dated the assembly and stabilization of Greenland. Such modification could occur as a result of the interaction of the lithosphere with hot sub-lithospheric mantle (Foley 2008).

The track of the Iceland hotspot is expected to cross Greenland, although its trajectory is uncertain (Forsyth *et al.* 1986; Lawver & Müller 1994; Lawver *et al.* 2002; Mihalffy *et al.* 2008; Ganerød *et al.* 2010; Torsvik *et al.* 2015). Near the eastern coast of Greenland, the observed corridor of thin lithosphere terminates where Torsvik *et al.* (2015) put the hotspot at 60–50 Ma. The Cape Hold With Hope – a location of basaltic volcanism attributed to the HALIP (e.g. Torsvik *et al.* 2015) – is just to the north. Just to the south along Greenland's coast, abundant basaltic volcanism occurred at the Blosseville Kyst; this is where the Iceland hotspot had moved (with Greenland as a reference) by 40 Ma, according to the reconstruction of Torsvik *et al.* (2015).

Near Greenland's western coast, the observed low-velocity corridor is roughly where Lawver & Müller (1994) placed the hotspot at 70 Ma – also close to the location of significant intraplate volcanism. The trend of the track of Lawver & Müller (1994) after 70 Ma is NW–SE, however, in contrast to the west–east trend of the corridor of thin lithosphere mapped here.

Yakovlev *et al.* (2012) inferred thinned lithosphere beneath parts of central Greenland from their regional travel-time P-wave tomography and attributed this to the passage of the area over the Iceland hotspot. In particular, they inferred thin lithosphere roughly beneath the eastern half of the area occupied by the corridor of thin lithosphere seen in our model (see also Petrunin *et al.* 2013). Steinberger *et al.* (2015) used global P-wave tomography (Bijwaard & Spakman 2000; Amaru 2007) and regional waveform tomography (Rickers *et al.* 2013) to argue that the lithosphere beneath eastern Greenland was thinned by thermal and mechanical erosion caused by the Iceland plume material underneath. Rogozhina *et al.* (2016) compared the P-wave (Yakovlev *et al.* 2012) and S-wave (Rickers *et al.* 2013) tomography, both displaying

low-velocity anomalies in the NW of Greenland, and various proposed hotspot tracks from plate reconstructions (Müller *et al.* 1993; Steinberger *et al.* 2004; O'Neill *et al.* 2005; Doubrovine *et al.* 2012) and inferred a location of the hotspot track from where we see the thinning at the east coast of Greenland towards the NW.

The well-defined corridor of thin lithosphere seen in our models is likely to show the complete extent of Greenland's lithospheric modification by the Iceland hotspot as the Greenland landmass moved across it. Unlike the previous seismology-inferred track locations, it connects the locations of abundant volcanism at the west and east coasts of Greenland. By contrast, the tomography models used by Rogozhina *et al.* (2016) suggest thick lithosphere beneath the volcanic areas on Greenland's western coast, which is difficult to reconcile with the voluminous volcanism in those areas. Our results thus provide important new evidence on the location of the hotspot track, from the east to the west of Greenland, and link plate motions over the Iceland hotspot with the spatial distribution of the volcanism.

Conclusions

Upper mantle tomography shows lateral variations in the temperature and thickness of the lithosphere. Because the variations in seismic velocities primarily reflect variations in temperature, tomographic maps offer a proxy for the lateral variations of temperature in the upper mantle.

New waveform tomography (Schaeffer & Lebedev 2015*b*; this study) provides improved resolution in the upper mantle of the Arctic, owing to the extensive waveform dataset used to construct the model – taking advantage of the recent expansion of broadband seismic networks around the region – and the elaborate waveform inversion and error analysis procedures.

Computational petrology enables self-consistent joint modelling and inversion of various geophysical and geological data. With informed assumptions about the composition of the lithosphere and asthenosphere and the parameters controlling anelasticity, seismic tomography models can be converted to thermal models of the upper mantle. A temperature estimate at a single point, however, may be biased due to the non-uniqueness of the three-dimensional tomographic models. Temperature averages over a depth range yield more robust and reliable temperature estimates. Our new map of the average temperature in the 80–150 km depth range shows the lateral thermal heterogeneity in the lithosphere–asthenoshere depth range across the Arctic region.

Our seismic and thermal models map the deep lithospheric boundaries of tectonic blocks with different properties and different ages – including cratons, Phanerozoic continents, the locations of intraplate volcanism and old and young oceans – and offer new insights into the dynamics and evolution of the Arctic lithosphere.

We thank the volume editor, Bernard Coakley and the reviewers, Alexander Minakov and Randell Stephenson, for helpful, constructive comments and suggestions. This work was supported by the Science Foundation Ireland (grants 13/CDA/2192 and 09/RFP/GEO2550) and the Natural Sciences and Engineering Research Council (NSERC) of Canada (Postdoctoral Fellowship to AS). The research leading to these results has received funding from the People Programme (Marie Curie Actions) of the European Union's H2020-MSCA-IF-2014 programme under REA grant agreement no. 657357 (grant awarded to JF). VP acknowledges funding from Swedish Research Council and CALE sponsors. All figures were implemented using Generic Mapping Tools (GMT, Wessel & Smith 1995).

References

Afonso, J.C. & Zlotnik, S. 2011. The subductability of the continental lithosphere: the before and after story. *In*: Brown, D. & Ryan, P.D. (eds) *Arc-Continent Collision*. Frontiers in Earth Sciences Series. Springer, Berlin, 53–86.

Afonso, J.C., Ranalli, G. & Fernàndez, M. 2005. Thermal expansivity and elastic properties of the lithospheric mantle: results from mineral physics of composites. *Physics of the Earth and Planetary Interiors*, **149**, 279–306.

Afonso, J.C., Fernàndez, M., Ranalli, G., Griffin, W.L. & Connolly, J.A.D. 2008. Integrated geophysical-petrological modeling of the lithosphere and sublithospheric upper mantle: methodology and applications. *Geochemistry, Geophysics, Geosystems*, **9**, Q05008, https://doi.org/10.1029/2007GC001834

Afonso, J.C., Fullea, J., Griffin, W.L., Yang, Y., Jones, A.G., Connolly, J.A.D. & O'Reilly, S.Y. 2013. 3-D multiobservable probabilistic inversion for the compositional and thermal structure of the lithosphere and upper mantle. I: a priori petrological information and geophysical observables. *Journal of Geophysical Research: Solid Earth*, **118**, 2586–2617.

Agius, M.R. & Lebedev, S. 2013. Tibetan and Indian lithospheres in the upper mantle beneath Tibet: evidence from broadband surface-wave dispersion. *Geochemistry, Geophysics, Geosystems*, **14**, 4260–4281.

Altenbernd, T., Jokat, W., Heyde, I. & Damm, V. 2016. Insights into the crustal structure of the transition between Nares Strait and Baffin Bay. *Tectonophysics*, https://doi.org/10.1016/j.tecto.2016.04.001

Amaru, M.L. 2007. *Global travel time tomography with 3-D reference models*. PhD thesis, Utrecht University.

Anell, I., Thybo, H. & Artemieva, I.M. 2009. Cenozoic uplift and subsidence in the North Atlantic region: geological evidence revisited. *Tectonophysics*, **474**, 78–105.

Artemieva, I.M. 2006. Global 1×1 thermal model TC1 for the continental lithosphere: implications for

lithosphere secular evolution. *Tectonophysics*, **416**, 245–277.

Artemieva, I.M., Thybo, H. & Kaban, M.K. 2006. Deep Europe today: geophysical synthesis of the upper mantle structure and lithospheric processes over 3.5 Ga. *In*: Gee, D.G. & Stephenson, R.A. (eds) *European Lithosphere Dynamics*. Geological Society, London, Memoirs, **32**, 11–41, https://doi.org/10.1144/GSL.MEM.2006.032.01.02

Auer, L., Boschi, L., Becker, T.W., Nissen-Meyer, T. & Giardini, D. 2014. Savani: a variable resolution whole-mantle model of anisotropic shear velocity variations based on multiple data sets. *Journal of Geophysical Research: Solid Earth*, **119**, 3006–3034.

Bartzsch, S., Lebedev, S. & Meier, T. 2011. Resolving the lithosphere–asthenosphere boundary with seismic Rayleigh waves. *Geophysical Journal International*, **186**, 1152–1164.

Bassin, C., Laske, G. & Masters, G. 2000. The current limits of resolution for surface wave tomography in North America. *Eos, Transactions of the American Geophysical Union*, **81**, F897.

Becker, T.W., Conrad, C.P., Schaeffer, A.J. & Lebedev, S. 2014. Origin of azimuthal seismic anisotropy in oceanic plates and mantle. *Earth and Planetary Science Letters*, **401**, 236–250.

Bijwaard, H. & Spakman, W. 2000. Non-linear global P-wave tomography by iterated linearized inversion. *Geophysical Journal International*, **141**, 71–82.

Bird, P. 1979. Continental delamination and the Colorado Plateau. *Journal of Geophysical Research*, **84**, 7561–7571.

Bruneton, M., Pedersen, H. *et al.* 2004. Complex lithospheric structure under the Central Baltic Shield from surface wave tomography. *Journal of Geophysical Research*, **109**, https://doi.org/10.1029/2003JB002947

Burgos, G., Montagner, J.P., Beucler, E., Capdeville, Y., Mocquet, A. & Drilleau, M. 2014. Oceanic lithosphere-asthenosphere boundary from surface wave dispersion data. *Journal of Geophysical Research: Solid Earth*, **119**, 1079–1093.

Burke, K. & Dewey, J.F. 1973. Plume-generated triple junctions: key indicators in applying plate tectonics to old rocks. *The Journal of Geology*, 406–433.

Burov, E.B. & Watts, A.B. 2006. The long-term strength of continental lithosphere: 'jelly sandwich' or 'crème brûlée'? *GSA Today*, **16**, 4.

Cammarano, F., Goes, S., Vacher, P. & Giardini, D. 2003. Inferring upper-mantle temperatures from seismic velocities. *Physics of the Earth and Planetary Interiors*, **138**, 197–222.

Cherepanova, Y. & Artemieva, I.M. 2015. Density heterogeneity of the cratonic lithosphere: a case study of the Siberian craton. *Gondwana Research*, **28**, 1344–1360.

Chian, D., Jackson, H.R. *et al.* 2016. Distribution of crustal types in Canada Basin, Arctic Ocean. *Tectonophysics*, https://doi.org/10.1016/j.tecto.2016.01.038

Coakley, B.J. & Cochran, J.R. 1998. Gravity evidence of very thin crust at the Gakkel Ridge (Arctic Ocean). *Earth and Planetary Science Letters*, **162**, 81–95.

Connolly, J.A.D. 2005. Computation of phase equilibria by linear programming: a tool for geodynamic modeling and its application to subduction zone decarbonation. *Earth and Planetary Science Letters*, **236**, 524–541.

Connolly, J.A.D. & Kerrick, D. 2002. Metamorphic controls on seismic velocity of subducted oceanic crust at 100–250 km depth. *Earth and Planetary Science Letters*, **204**, 61–74.

Davis, E.E. & Lister, C.R.B. 1974. Fundamentals of ridge crest topography. *Earth and Planetary Science Letters*, **21**, 405–413.

Dawes, P.R. & Kerr, J.W. (eds) 1982. *Nares Strait and the Drift of Greenland: a Conflict in Plate Tectonics*. Meddelelser om Grønland Geosciences, **8**.

Dawes, P.R., Frisch, T. & Christie, R.L. 1982. The Proterozoic Thule Basin of Greenland and Ellesmere Island: importance to the Nares Strait debate. *In*: Dawes, P.R. & Kerr, J.W. (eds) *Nares Strait and the Drift of Greenland: a Conflict in Plate Tectonics*. Meddelelser om Grønland Geosciences, **8**, 89–104.

Debayle, E., Dubuffet, F. & Durand, S. 2016. An automatically updated S-wave model of the upper mantle and the depth extent of azimuthal anisotropy. *Geophysical Research Letters*, **43**, https://doi.org/10.1002/2015GL067329

Deschamps, P., Trampert, J. & Snieder, R. 2002. Anomalies of temperature and iron in the uppermost mantle inferred from gravity data and tomographic models. *Physics of the Earth and Planetary Interiors*, **129**, 245–264.

Dobretsov, N.L., Vernikovsky, V.A., Karyakin, Y.V., Korago, E.A. & Simonov, V.A. 2013. Mesozoic–Cenozoic volcanism and geodynamic events in the Central and Eastern Arctic. *Russian Geology and Geophysics*, **54**, 874–887.

Doubrovine, P.V., Steinberger, B. & Torsvik, T.H. 2012. Absolute plate motions in a reference frame defined by moving hot spots in the Pacific, Atlantic, and Indian oceans. *Journal of Geophysical Research: Solid Earth*, **117**, https://doi.org/10.1029/2011JB009072

Drachev, S. & Saunders, A. 2006. The early Cretaceous Arctic LIP: its geodynamic setting and implications for Canada Basin opening. *In*: Scott, R.A. & Thurston, D. (eds) *ICAM IV Proceedings*. US Department of the Interior, Anchorage, AK, 216–223.

Eaton, D.W., Darbyshire, F., Evans, R.L., Grütter, H., Jones, A.G. & Yuan, X. 2009. The elusive lithosphere–asthenosphere boundary (LAB) beneath cratons. *Lithos*, **109**, 1–22.

Embry, A. & Beauchamp, B. 2008. *Sverdrup Basin*. Sedimentary Basins of the World, **5**. Elsevier, Amsterdam, 451–471.

Foley, S.F. 2008. Rejuvenation and erosion of the cratonic lithosphere. *Nature Geoscience*, **1**, 503–510.

Forsyth, D.A., Asudeh, I., Green, A.G. & Jackson, H.R. 1986. Crustal structure of the northern Alpha Ridge beneath the Arctic Ocean. *Nature*, **322**, 349–352.

French, S., Lekic, V. & Romanowicz, B. 2013. Waveform tomography reveals channeled flow at the base of the oceanic asthenosphere. *Science*, **342**, 227–230.

Fullea, J., Afonso, J.C., Connolly, J.A.D., Fernández, M., García-Castellanos, D. & Zeyen, H. 2009. LitMod3D: an interactive 3-D software to model the thermal, compositional, density, seismological, and

rheological structure of the lithosphere and sublithospheric upper mantle. *Geochemistry, Geophysics, Geosystems*, **10**, Q08019, https://doi.org/10.1029/2009GC002391

Fullea, J., Lebedev, S., Agius, M.R., Jones, A.G. & Afonso, J.C. 2012. Lithospheric structure in the Baikal–central Mongolia region from integrated geophysical-petrological inversion of surface-wave data and topographic elevation. *Geochemistry, Geophysics, Geosystems*, **13**, Q0AK09, https://doi.org/10.1029/2012GC004138

Gaina, C., Medvedev, S., Torsvik, T.H., Koulakov, I. & Werner, S.C. 2014. 4D Arctic: a glimpse into the structure and evolution of the arctic in the light of new geophysical maps, plate tectonics and tomographic models. *Surveys in Geophysics*, **35**, 1095–1122.

Gaina, C., Nikishin, A.M. & Petrov, E.I. 2015. Ultraslow spreading, ridge relocation and compressional events in the East Arctic region: a link to the Eurekan orogeny? *Arktos*, **1**, 16, https://doi.org/10.1007/s41063-015-0006-8.

Ganerød, M., Smethurst, M.A. *et al*. 2010. The North Atlantic Igneous Province reconstructed and its relation to the plume generation zone: the Antrim lava group revisited. *Geophysical Journal International*, **182**, 183–202.

Goes, S., Govers, R. & Vacher, P. 2000. Shallow mantle temperatures under Europe from P and S wave tomography. *Journal of Geophysical Research*, **105**, 11153–11169.

Grantz, A., Hart, P. & Childers, V. 2011. Geology and tectonic development of the Amerasia and Canada Basins, Arctic Ocean. *In*: Spencer, A.M., Embry, A.F., Gautier, D.L., Stoupakova, A.V. & Sørensen, K. (eds) *Arctic Petroleum Geology*. Geological Society, London, Memoirs, **35**, 771–799, https://doi.org/10.1144/M35.50

Griffin, W.L., O'Reilly, S.Y., Afonso, J.C. & Begg, G. 2009. The composition and evolution of lithospheric mantle: a re-evaluation and its tectonic implications. *Journal of Petrology*, **50**, 1185–1204.

Hammond, W.C. & Humphreys, E.D. 2000. Upper mantle seismic wave velocity: effects of realistic partial melt geometries. *Journal of Geophysical Research: Solid Earth*, **105**, 10975–10986.

Herron, E.M., Dewey, J.F. & Pitman, W.C. 1974. Plate tectonics model for the evolution of the Arctic. *Geology*, **2**, 377–380.

Holland, T.J.B. & Powell, R. 1998. An internally consistent thermodynamic data set for phases of petrological interest. *Journal of Metamorphic Geology*, **16**, 309–343.

Houseman, G.A. & Molnar, P. 1997. Gravitational (Rayleigh–Taylor) instability of a layer with nonlinear viscosity and convective thinning of continental lithosphere. *Geophysical Journal International*, **128**, 125–150.

Jakobsson, M., Mayer, L. *et al*. 2012. The international bathymetric chart of the Arctic Ocean (IBCAO) version 3.0. *Geophysical Research Letters*, **39**, L12609, https://doi.org/10.1029/2012GL052219

Jaupart, C. & Mareschal, J.C. 1999. The thermal structure and thickness of continental roots. *Lithos*, **48**, 93–114.

Jokat, W., Ritzmann, O., Schmidt-Aursch, M.C., Drachev, S., Gauger, S. & Snow, J. 2003. Geophysical evidence for reduced melt production on the Arctic ultraslow Gakkel mid-ocean ridge. *Nature*, **423**, 962–M965.

Jordan, T.H. 1975. The continental tectosphere. *Revies in Geophysics*, **13**, 1–12.

Jordan, T.H. 1988. Structure and formation of the continental tectosphere. *Journal of Petrology*, **1**, 11–37.

Karato, S.I. 1993. Importance of anelasticity in the interpretation of seismic tomography. *Geophysical Research Letters*, **20**, 1623–1626.

Katz, R.F., Spiegelman, M. & Langmuir, C.H. 2003. A new parameterization of hydrous mantle melting. *Geochemistry, Geophysics, Geosystems*, **4**, 1073, https://doi.org/10.1029/2002GC000433

Khan, A., Boschi, L. & Connolly, J.A.D. 2009. On mantle chemical and thermal heterogeneities and anisotropy as mapped by inversion of global surface wave data. *Journal of Geophysical Research: Solid Earth*, **114**, B09305.

Khan, A., Boschi, L. & Connolly, J.A.D. 2011. Mapping the Earth's thermochemical and anisotropic structure using global surface wave data. *Journal of Geophysical Research: Solid Earth*, **116**, B01301.

Koulakov, I.Y., Gaina, C., Dobretsov, N.L., Vasilevsky, A.N. & Bushenkova, N.A. 2013. Plate reconstructions in the Arctic region based on joint analysis of gravity, magnetic, and seismic anomalies. *Russian Geology and Geophysics*, **54**, 859–873.

Kuskov, O.L., Kronrod, V.A., Prokofyev, A.A. & Pavlenkova, N.I. 2014. Thermo-chemical structure of the lithospheric mantle underneath the Siberian craton inferred from long-range seismic profiles. *Tectonophysics*, **615**, 154–166.

Kuzmichev, A.B. & Pease, V.L. 2007. Siberian trap magmatism on the New Siberian Islands: constraints for Arctic Mesozoic plate tectonic reconstructions. *Journal of the Geological Society*, **164**, 959–968, https://doi.org/10.1144/0016-76492006-090

Lane, L.S. 1997. Canada Basin, Arctic Ocean: evidence against a rotational origin. *Tectonics*, **5**, 252–276.

Lawver, L.A. & Müller, R.D. 1994. Iceland hotspot track. *Geology*, **22**, 311–314.

Lawver, L.A. & Scotese, C.R. 1990. A review of tectonic models for the evolution of the Canada Basin. *In*: Grantz, A., Johnson, G.L. & Sweeney, J.F. (eds) *The Arctic Ocean Region*. The Geology of North America, L. Geological Society of America, Boulder, CO, 593–618.

Lawver, L.A., Grantz, A. & Gahagan, L.M. 2002. Plate kinematic evolution of the present Arctic region since the Ordovician. *In*: Miller, E.L., Grantz, A. & Klemperer, S.L. (eds) *Tectonic Evolution of the Bering Shelf–Chukchi Sea–Artic Margin and Adjacent Landmasses*. Geological Society of America, Special Papers, **360**, 333–358.

Lebedev, S. & Nolet, G. 2003. Upper mantle beneath Southeast Asia from S velocity tomography. *Journal of Geophysical Research: Solid Earth*, **108**, 2048, https://doi.org/10.1029/2000JB000073

Lebedev, S. & van der Hilst, R.D. 2008. Global upper-mantle tomography with the automated multimode

inversion of surface and S-wave forms. *Geophysical Journal International*, **173**, 505–518.

Lebedev, S., Nolet, G. & Van Der Hilst, R.D. 1997. The upper mantle beneath the Philippine Sea region from waveform inversions. *Geophysical Research Letters*, **24**, 1851–1854.

Lebedev, S., Nolet, G., Meier, T. & van der Hilst, R.D. 2005. Automated multimode inversion of surface and *S* waveforms. *Geophysical Journal International*, **162**, 951–964.

Lebedev, S., Meier, T. & van der Hilst, R.D. 2006. Asthenospheric flow and origin of volcanism in the Baikal Rift area. *Earth and Planetary Science Letters*, **249**, 415–424.

Lebedev, S., Boonen, J. & Trampert, J. 2009. Seismic structure of Precambrian lithosphere: new constraints from broad-band surface-wave dispersion. *Lithos*, **109**, 96–111.

Lebedev, S., Adam, J.M.C. & Meier, T. 2013. Mapping the Moho with seismic surface waves: a review, resolution analysis, and recommended inversion strategies. *Tectonophysics*, **609**, 377–394.

Legendre, C.P., Meier, T., Lebedev, S., Friederich, W. & Viereck-Götte, L. 2012. A shear wave velocity model of the European upper mantle from automated inversion of seismic shear and surface waveforms. *Geophysical Journal International*, **191**, 282–304.

Lekic, V. & Romanowicz, B. 2011. Tectonic regionalization without a priori information: a cluster analysis of upper mantle tomography. *Earth and Planetary Science Letters*, **308**, 151–160.

Levshin, A.L., Ritzwoller, M.H., Barmin, M.P., Villasenor, A. & Padgett, C.A. 2001. New constraints on the Arctic crust and uppermost mantle: surface wave group velocities, Pn, and Sn. *Physics of the Earth and Planetary Interiors*, **123**, 185–204.

Levshin, A.L., Schweitzer, J., Weidle, C., Shapiro, N.M. & Ritzwoller, M.H. 2007. Surface wave tomography of the Barents Sea and surrounding regions. *Geophysical Journal International*, **170**, 441–459.

Maggi, A., Debayle, E., Priestley, K. & Barruol, G. 2006. Multimode surface waveform tomography of the Pacific Ocean: a closer look at the lithospheric cooling signature. *Geophysical Journal International*, **166**, 1384–1397.

Maupin, V., Agostini, A. *et al.* 2013. The deep structure of the Scandes and its relation to tectonic history and present-day topography. *Tectonophysics*, **602**, 15–37.

McDonough, W.F. & Sun, S.-S. 1995. The composition of the Earth. *Chemical Geology*, **120**, 223–253.

McKenzie, D., Jackson, J. & Priestley, K. 2005. Thermal structure of oceanic and continental lithosphere. *Earth and Planetary Science Letters*, **233**, 337–349.

Meier, T., Soomro, R. *et al.* 2016. Mesozoic and Cenozoic evolution of the central European lithosphere. *Tectonophysics*, **692**, 58–73.

Menzies, M.A., Fan, W. & Zhang, M. 1993. Palaeozoic and Cenozoic lithoprobes and the loss of >120 km of Archaean lithosphere, Sino-Korean craton, China. *In*: Prichard, H.M., Alabaster, T., Harris, N.B.W. & Neary, C.R. (eds) *Magmatic Processes and Plate Tectonics*. Geological Society, London, Special Publications, **76**, 71–81, https://doi.org/10.1144/GSL.SP.1993.076.01.04

Michael, P.J., Langmuir, C.H. *et al.* 2003. Magmatic and amagmatic seafloor generation at the ultraslow-spreading Gakkel Ridge, Arctic Ocean. *Nature*, **423**, 956–961.

Midwinter, D., Hadlari, T., Davis, W.J., Dewing, K. & Arnott, R.W.C. 2016. Dual provenance signatures of the Triassic northern Laurentian margin from detrital-zircon U–Pb and Hf-isotope analysis of Triassic–Jurassic strata in the Sverdrup Basin. *Lithosphere*, https://doi.org/10.1130/L517.1

Mihalffy, P., Steinberger, B. & Schmeling, H. 2008. The effect of the large-scale mantle flow field on the Iceland hotspot track. *Tectonophysics*, **447**, 5–18.

Minster, J.B. & Anderson, D.L. 1981. A model of dislocation-controlled rheology for the mantle. *Philosophical Transactions of the Royal Society of London Series A*, **299**, 319–356.

Morgan, W.J. & Morgan, J.P. 2005. Volcanism due to horizontal sublithospheric flow. Paper presented at the 4th Deep Earth: Theory, Experiment and Observation Research Conference, Lithosphere–Asthenosphere Interaction, 28 May–1 June, 2005, Frejus, France.

Mosher, D.C., Shimeld, J., Hutchinson, D., Chian, D., Lebedova-Ivanova, & Jackson, R. 2012. Canada Basin revealed. Paper presented at the OTC Arctic Technology Conference, 3–5 December 2012, Houston, Texas, USA, OTC 23797.

Müller, R.D., Royer, J.Y. & Lawver, L.A. 1993. Revised plate motions relative to the hotspots from combined Atlantic and Indian Ocean hotspot tracks. *Geology*, **21**, 275–278.

Nolet, G. 1990. Partitioned waveform inversion and two-dimensional structure under the network of autonomously recording seismographs. *Journal of Geophysical Research: Solid Earth*, **95**, 8499–8512.

Oakey, G.N. & Chalmers, J.A. 2012. A new model for the Paleogene motion of Greenland relative to North America: plate reconstructions of the Davis Strait and Nares Strait regions between Canada and Greenland. *Journal of Geophysical Research: Solid Earth*, **117**, https://doi.org/10.1029/2011JB008942

O'Neill, C., Müller, D. & Steinberger, B. 2005. On the uncertainties in hot spot reconstructions and the significance of moving hot spot reference frames. Geochemistry, Geophysics, Geosystems, 6(4). Pease, V. 2011. Eurasian orogens and Arctic tectonics: an overview. *In*: Spencer, A.M., Embry, A.F., Gautier, D.L., Stoupakova, A.V. & Sørensen, K. (eds) *Arctic Petroleum Geology*. Geological Society, London, Memoirs, **35**, 311–324, https://doi.org/10.1144/M35.20

Pease, V. 2011. Eurasian orogens and Arctic tectonics: an overview. *In*: Spencer, A.M., Embry, A.F., Gautier, D.L., Stoupakova, A.V. & Sørensen, K. (eds) *Arctic Petroleum Geology*. Geological Society, London, Memoirs, **35**, 311–324, https://doi.org/10.1144/M35.20

Pease, V., Drachev, S., Stephenson, R. & Zhang, X. 2014. Arctic lithosphere – a review. *Tectonophysics*, **628**, 1–25.

Pedersen, H., Debayle, E. & Maupin, V. 2013. Strong lateral variations of lithospheric mantle beneath cratons – example from the Baltic Shield. *Earth and Planetary Science Letters*, **383**, 164–172.

Petrov, O., Morozov, A. *et al.* 2016. Crustal structure and tectonic model of the Arctic region. *Earth-Science Reviews*, **154**, 29–71.

Petrunin, A.G., Rogozhina, I., Vaughan, A.P.M., Kukkonen, I.T., Kaban, M.K., Koulakov, I. & Thomas, M. 2013. Heat flux variations beneath central Greenland's ice due to anomalously thin lithosphere. *Nature Geoscience*, **6**, 746–750.

Piepjohn, K., von Gosen, W. *et al.* 2015. Tectonic map of the Ellesmerian and Eurekan deformation belts on Svalbard, North Greenland, and the Queen Elizabeth Islands (Canadian Arctic). *Arktos*, **1**, 12, https://doi.org/10.1007/s41063-015-0015-7

Pollack, H.N. & Chapman, D.S. 1977. On the regional variation of heat flow, geotherms, and lithospheric thickness. *Tectonophysics*, **38**, 279–296.

Poudjom Djomani, Y.H., O'Reilly, S.Y., Griffin, W.L. & Morgan, P. 2001. The density structure of subcontinental lithosphere through time. *Earth and Planetary Science Letters*, **184**, 605–621.

Reichow, M.K., Saunders, A.D., White, R.V., Pringle, M.S., Al'Mukhamedov, A.I., Medvedev, A.I. & Kirda, N.P. 2002. $^{40}Ar/^{39}Ar$ dates from the West Siberian Basin: Siberian flood basalt province doubled. *Science*, **296**, 1846–1849.

Renne, P.R. & Basu, A.R. 1991. Rapid eruption of the Siberian Traps flood basalts at the Permo-Triassic boundary. *Science*, **253**, 176–179.

Rickers, F., Fichtner, A. & Trampert, J. 2013. The Iceland–Jan Mayen plume system and its impact on mantle dynamics in the North Atlantic region: evidence from full-waveform inversion. *Earth and Planetary Science Letters*, **367**, 39–51.

Ritsema, J., Deuss, A., van Heijst, H.J. & Woodhouse, J.H. 2011. S40RTS: a degree-40 shear-velocity model for the mantle from new Rayleigh wave dispersion, teleseismic traveltime and normal-mode splitting function measurements. *Geophysical Journal International*, **184**, 1223–1236.

Rogozhina, I., Petrunin, A.G. *et al.* 2016. Melting at the base of the Greenland ice sheet explained by Iceland hotspot history. *Nature Geoscience*, **9**, 366–369.

Saalmann, K., Tessensohn, F., Piepjohn, K., Von Gosen, W. & Mayr, U. 2005. Structure of Palaeogene sediments in east Ellesmere Island: constraints on Eurekan tectonic evolution and implications for the Nares Strait problem. *Tectonophysics*, **406**, 81–113.

Saumur, B.M., Dewing, K. & Williamson, M.C. 2016. Architecture of the Canadian portion of the High Arctic Large Igneous Province and implications for magmatic Ni–Cu potential. *Canadian Journal of Earth Sciences*, **53**, 528–542.

Schaeffer, A.J. & Lebedev, S. 2013. Global shear-speed structure of the upper mantle and transition zone. *Geophysical Journal International*, **194**, 417–449.

Schaeffer, A.J. & Lebedev, S. 2014. Imaging the North American continent using waveform inversion of global and USArray data. *Earth and Planetary Science Letters*, **402**, 26–41.

Schaeffer, A.J. & Lebedev, S. 2015*a*. Global heterogeneity of the lithosphere and underlying mantle: a seismological appraisal based on multimode surface-wave dispersion analysis, shear-velocity tomography, and tectonic regionalization. *In*: Khan, A. & Deschamps, F. (eds) *The Earth's Heterogeneous Mantle*. Springer Geophysics Series. Springer, Berlin, https://doi.org/10.1007/978-3-319-15627-9_1, 3–46

Schaeffer, A.J. & Lebedev, S. 2015*b*. Seismic tomography of the Arctic lithosphere and asthenosphere. Paper presented at the EGU General Assembly Conference, 12–17 April 2015, Vienna, Austria, **17**, 2819.

Schaeffer, A.J., Lebedev, S. & Becker, T.W. 2016. Azimuthal seismic anisotropy in the Earth's upper mantle and the thickness of tectonic plates. *Geophysical Journal International*, **207**, 901–933.

Schiffer, C. & Stephenson, R. 2017. Regional crustal architecture of Ellesmere Island, Arctic Canada. *In*: Pease, V. & Coakley, B. (eds) *Circum-Arctic Lithosphere Evolution*. Geological Society, London, Special Publications, **460**. First published online June 12, 2017, https://doi.org/10.1144/SP460.8

Schiffer, C., Tegner, C., Schaeffer, A.J., Pease, V. & Nielsen, S.B. 2017. High Arctic geopotential stress field and implications for the geodynamic evolution. Pease, V. & Coakley, B. (eds) *Circum-Arctic Lithosphere Evolution*. Geological Society, London, Special Publications, **460**. First published online April 13, 2017, https://doi.org/10.1144/SP460.6

Schlindwein, V., Müller, C. & Jokat, W. 2007. Microseismicity of the ultraslow-spreading Gakkel ridge, Arctic Ocean: a pilot study. *Geophysical Journal International*, **169**, 100–112.

Schmidt-Aursch, M.C. & Jokat, W. 2016. 3D gravity modelling reveals off-axis crustal thickness variations along the western Gakkel Ridge (Arctic Ocean). *Tectonophysics*, **691**, 85–97.

Schutt, D.L. & Lesher, C.E. 2006. Effects of melt depletion on the density and seismic velocity of garnet and spinel lherzolite. *Journal of Geophysical Research*, **111**, https://doi.org/10.1029/2003JB002950

Shapiro, N.M. & Ritzwoller, M.H. 2002. Monte-Carlo inversion for a global shear-velocity model of the crust and upper mantle. *Geophysical Journal International*, **151**, 88–105.

Sobolev, S.V., Zeyen, H., Stoll, G., Werling, F., Altherr, R. & Fuchs, K. 1996. Upper mantle temperatures from teleseismic tomography of French Massif Central including effects of composition, mineral reactions, anharmonicity, anelasticity and partial melt. *Earth and Planetary Science Letters*, **139**, 147–163.

Sobolev, S.V., Sobolev, A.V. *et al.* 2011. Linking mantle plumes, large igneous provinces and environmental catastrophes. *Nature*, **477**, 312–316.

Sodoudi, F., Yuan, X., Kind, R., Lebedev, S., Adam, J.M.C., Kästle, E. & Tilmann, F. 2013. Seismic evidence for stratification in composition and anisotropic fabric within the thick lithosphere of Kalahari Craton. *Geochemistry, Geophysics, Geosystems*, **14**, 5393–5412.

Stein, C.A. & Stein, S. 1992. A model for the global variation in oceanic depth and heat flow with lithospheric age. *Nature*, **359**, 123–129.

Stein, C.A. & Stein, S. 2015. Are large oceanic depth anomalies caused by thermal perturbations? *In*: Foulger, G.R., Lustrino, M. & King, S.D. (eds) *The Interdisciplinary Earth: A Volume in Honor of Don L. Anderson*. Geological Society of America, Special Papers, **514** and American Geophysical Union, Special Publications, **71**, https://doi.org/10.1130/2015.2514(12)

Steinberger, B., Sutherland, R. & O'Connell, R.J. 2004. Prediction of Emperor-Hawaii seamount locations from a revised model of global plate motion and mantle flow. *Nature*, **430**, 167–173.

Steinberger, B., Spakman, W., Japsen, P. & Torsvik, T.H. 2015. The key role of global solid-Earth processes in preconditioning Greenland's glaciation since the Pliocene. *Terra Nova*, **27**, 1–8.

Stephenson, R.A., Embry, A.F., Nakiboglu, S.M. & Hastaoglu, M.A. 1987. Rift-initiated Permian to Early Cretaceous subsidence of the Sverdrup basin. *In*: Beaumont, C. & Tankard, A.J. (eds) *Sedimentary Basins and Basin-Forming Mechanisms*. Canadian Society of Petroleum Geologists, Memoirs, **12**, 213–231.

Stephenson, R.A. *et al.* 2017. Integrated crustal–geological cross-section of Ellesmere Island. *In*: Pease, V. & Coakley, B. (eds) *Circum-Arctic Lithosphere Evolution*. Geological Society, London, Special Publications, **460**. First published online May 23, 2017, https://doi.org/10.1144/SP460.12

St-Onge, M.R., Van Gool, J.A., Garde, A.A. & Scott, D.J. 2009. Correlation of Archaean and Palaeoproterozoic units between northeastern Canada and western Greenland: constraining the pre-collisional upper plate accretionary history of the Trans-Hudson orogen. *In*: Cawood, P.A. & Kröner, A. (eds) *Earth Accretionary Systems in Space and Time*. Geological Society, London, Special Publications, **318**, 193–235, https://doi.org/10.1144/SP318.7

Tarduno, J.A. 1998. The high Arctic large igneous province. Paper presented at the Third International Conference on Arctic Margins, Celle, Germany, 12–15 October 1998, 12–16.

Thiede, J. & the Shipboard Scientific Party 2002. Cruise Report: AMORE2001. *Reports on Polar Marine Research*, **421**. Alfred-Wegener-Institut, Bremerhaven.

Thompson, R.N. & Gibson, S.A. 1991. Subcontinental mantle plumes, hotspots and pre-existing thinspots. *Journal of the Geological Society*, **148**, 973–977, https://doi.org/10.1144/gsjgs.148.6.0973

Torsvik, T.H. 2016. Earth evolution and dynamics (Arthur Holmes Medal Lecture). Paper presented at the EGU General Assembly Conference, 17–22 April 2016, Vienna, Austria, Vol. **18**, 1458.

Torsvik, T.H., Amundsen, H.E. *et al.* 2015. Continental crust beneath southeast Iceland. *Proceedings of the National Academy of Sciences of the USA*, **112**, E1818–E1827.

Torsvik, T.H., Steinberger, B., Ashwal, L.D., Doubrovine, P.V. & Trønnes, R.G. 2016. Earth evolution and dynamics – a tribute to Kevin Burke 1. *Canadian Journal of Earth Sciences*, **53**, 1073–1087.

Vozar, J., Jones, A.G., Fullea, J., Agius, M.R., Lebedev, S., Le Pape, F. & Wei, W. 2014. Integrated geophysical–petrological modeling of lithosphere–asthenosphere boundary in central Tibet using electromagnetic and seismic data. *Geochemistry, Geophysics, Geosystems*, **15**, 3965–3988.

Wessel, P. & Smith, W.H. 1995. New version of the generic mapping tools. *Eos, Transactions American Geophysical Union*, **76**, 329–329.

Wegener, A. 1929 (1966). *The Origin of Continents and Oceans*. 4th edn. Dover, New York.

Weidle, C. & Maupin, V. 2008. An upper-mantle S-wave velocity model for Northern Europe from Love and Rayleigh group velocities. *Geophysical Journal International*, **175**, 1154–1168.

White, N. & Lovell, B. 1997. Measuring the pulse of a plume with the sedimentary record. *Nature*, **387**, 888–891.

Wilson, J.T. 1963. Hypothesis of Earth's behaviour. *Nature*, **198**, 925–929.

Yakovlev, A.V., Bushenkova, N.A., Koulakov, I.Y. & Dobretsov, N.L. 2012. Structure of the upper mantle in the Circum-Arctic region from regional seismic tomography. *Russian Geology and Geophysics*, **53**, 963–971.